Soil Moisture Memory in Commonly-used Land Surface Models Differ Significantly from SMAP Observation

He Qing[1], Lu Hui[1], and Yang Kun[1]

[1]Department of Earth System Science, Tsinghua University

November 16, 2022

Abstract

Weather and climate forecast predictability relies on Land-Atmosphere (L-A) interactions occurring at different time scales. However, evaluation of L-A coupling parameterizations in current land surface models (LSMs) is challenging since the physical processes are complex, and large-scale observations are scarce and uncommon. Recent advancements in satellite observations, in this light, provide a unique opportunity to evaluate the models' performances at large spatial scales. Using 5-year soil moisture memory (SMM) from Soil Moisture Active and Passive (SMAP) observations, we evaluate L-A coupling performances in 4 prevailing LSMs with both coupled and offline simulations. Multi-model mean comparison at the global scale shows that current LSMs tend to overestimate SMM that is controlled by water-limited processes and vice versa. Large model spreads in SMM are also observed between individual models. The SMM biases are highly dependent on models' parameterizations, while showing minor relevance to the models' soil layer depths or the models' online/offline simulating schemes. Further analyses of two important terrestrial water cycle-related variables indicate current LSMs may underestimate soil moisture that is directly available for evapotranspiration and global flood risks. Finally, a comparison of two soil moisture thresholds indicates that the soil parameters employed in LSMs play an essential role in producing the model's biases. The satellite estimation of ET at the water-limited stage and soil hydraulic parameters provides readily available information to constrain LSMs, which are essentially important to improve the models' L-A coupling simulations, as well as other land surface processes such as terrestrial hydrological cycles.

Soil Moisture Memory in Commonly-used Land Surface Models Differ Significantly from SMAP Observation

Qing He[1], Hui Lu[1,2] and Kun Yang[1]

[1]Ministry of Education Key Laboratory for Earth System Modeling and the Department of Earth System Science, Tsinghua University, Beijing, 100084, China

[2]Ministry of Education Ecological Field Station for East Asian Migratory Birds, Beijing, 100084, China

Corresponding author: Hui Lu (luhui@tsinghua.edu.cn)

Key Points:

- The four prevailing LSMs show similar misestimation of soil moisture memory compared to SMAP observation.
- The differences between LSMs and SMAP are highly dependent on the models' parameterizations.
- The soil parameters may play an essential role in determining the LSMs' L-A coupling biases.

Abstract

Weather and climate forecast predictability relies on Land-Atmosphere (L-A) interactions occurring at different time scales. However, evaluation of L-A coupling parameterizations in current land surface models (LSMs) is challenging since the physical processes are complex, and large-scale observations are scarce and uncommon. Recent advancements in satellite observations, in this light, provide a unique opportunity to evaluate the models' performances at large spatial scales. Using 5-year soil moisture memory (SMM) from Soil Moisture Active and Passive (SMAP) observations, we evaluate L-A coupling performances in 4 prevailing LSMs with both coupled and offline simulations. Multi-model mean comparison at the global scale shows that current LSMs tend to overestimate SMM that is controlled by water-limited processes and vice versa. Large model spreads in SMM are also observed between individual models. The SMM biases are highly dependent on models' parameterizations, while showing minor relevance to the models' soil layer depths or the models' online/offline simulating schemes. Further analyses of two important terrestrial water cycle-related variables indicate current LSMs may underestimate soil moisture that is directly available for evapotranspiration and global flood risks. Finally, a comparison of two soil moisture thresholds indicates that the soil parameters employed in LSMs play an essential role in producing the model's biases. The satellite estimation of ET at the water-limited stage and soil hydraulic parameters provides readily available information to constrain LSMs, which are essentially important to improve the models' L-A coupling simulations, as well as other land surface processes such as terrestrial hydrological cycles.

Plain Language Summary

To have a more accurate weather forecast, a better description of physical processes between Land and Atmosphere (L-A) is required. The L-A processes are often characterized by Land Surface Models (LSMs). However, because such processes are complex, and the observation records are scarce, it is difficult to evaluate the L-A simulations in current LSMs on large scale. Recent advances in satellite technology provide a unique opportunity to evaluate the LSMs' performances on basis of observed evidence.

In this study, we use SMAP-observed SMM to evaluate the four most widely-used LSMs. Results show that the four LSMs tend to overestimate SMM that is controlled by the water-limited processes and vice versa. Large differences between models are observed, showing high dependence on the model's parameterizations. Two water cycle-related variables are also analyzed, indicating the LSMs may underestimate soil moisture that is directly available for evapotranspiration and global flood risks. Finally, a comparison of the models' soil parameters shows that these parameters play an essential role in producing the models' biases. This study provides a comprehensive evaluation of L-A simulating performances in several prevailing LSMs. This study also provides useful information to constrain LSMs, which are important to improve Earth's land surface simulations.

1 Introduction

Land-atmosphere (L-A) interactions occurring at different timescales are important for regional weather and climate (Seneviratne et al., 2010). For example, the coupling of surface water and temperature anomalies can intensify the evolutions of extreme events such as droughts and heatwaves (Koster et al., 2009; Miralles et al., 2019, 2014; Seneviratne et al., 2006). However, the L-A coupling processes are complex and often interact with each other. As such, current climate models often present large model uncertainties in characterizing L-A coupling strength, for example, previous studies have shown that there are large differences between soil moisture (SM) and precipitation coupling strength in several prevalently-used global climate models (Guo et al., 2006; Koster et al., 2006, 2002). Similar model spreads are also found in coupling strength between SM and evapotranspiration (ET)(Berg and Sheffield, 2018; Dirmeyer et al., 2006). However, since large-scale observations of essential L-A variables (e.g., SM and ET) are scarce (Pastorello et al., 2020; Seneviratne et al., 2010), recent assessments are limited to inter-model comparisons only. However, in order to improve the models' L-A coupling performance, it is essentially important to diagnose individual models' biases with observational evidence. In this light, recent advances in satellite technologies provide unique opportunities to investigate L-A coupling processes at large spatial scales.

A diversity of methods have been developed to characterize L-A coupling strength, where algorithms based on sensitivity analyses, e.g., correlation and covariance analyses (Dirmeyer, 2011; Dirmeyer et al., 2009; Miralles et al., 2014), and partial differentiation between multiple L-A variables (Feldman et al., 2019; Gallego-Elvira et al., 2016; Schwingshackl et al., 2017), are favored since they present explicit physical indications to understand. However, since the sensitivity analyses require at least two L-A variables, it is even more challenging to obtain observational records at large spatial scales. By contrast, soil moisture memory (SMM) – an L-A coupling metric that is based solely on SM time series – could facilitate L-A coupling assessment studies for less dependence on data availability, especially when a large number of models are analyzed (e.g., common variables should be selected when using multi-variable analyses, which may reduce the model numbers; using SMM instead can efficiently avoid this problem).

SMM measures the time when soil moisture recovers to equilibrium from perturbations (a perturbation can refer to either a wet anomaly such as precipitation or a dry anomaly such as drought). Methods such as e-folding time based on the Markov process (Delworth and Manabe, 1988; Koster and Suarez, 2001) and time scale based on soil moisture integral (Ghannam et al., 2016; Katul et al., 2007) are developed to quantify SMM. In these studies, shorter SMM time indicates more rapid water and energy exchanges between land and near-surface atmosphere – thus stronger L-A coupling strength. However, while the methods based on Markov processes provide overall L-A coupling indications, they do not characterize land processes occurring at different time scales (e.g., drainage occuring within hours or days and ET processes occuring at subweekly to weekly after precipitation events). In other words, SMM based on Markov processes does not provide explicit physical indications for calibrating models' parameterizations. A recently developed hybrid model does so by separating the effects of water- and energy-limitations on surface processes (McColl et al., 2019). By comparing the satellite estimates with one example land surface model (LSM), the study demonstrates that the LSM tends to overestimate SMM time at long-term scales whereas underestimates SMM at short-term time scales.

However, it is still unknown whether the above conclusion is a common nature in most LSMs – the L-A coupling parameterization schemes in LSMs are usually highly model-dependent, and can be susceptible to individual models' configurations, e.g., soil layer depth, online/offline simulating schemes, critical L-A parameters, etc. Moreover, in McColl et al. (2019) the satellite-based SMM are estimated from single-year soil moisture time series due to limitations in data availability. However, the annual variability of soil moisture could influence the conclusions. In this light, multi-model assessments of L-A coupling characteristics at different time scales are necessary to diagnose biases and further provide a reference to improve L-A coupling simulations in current LSMs.

In this study, we provide a comprehensive evaluation of L-A coupling characteristics in several prevalently-used LSMs (i.e., Noah LSM, Catchment LSM, HTESSEL and SiB) by using SMM estimated from 5-year satellite observations. We intend to address the two following questions: (1) Compared to large-scale satellite observations, how do the prevailing LSMs perform in simulating L-A coupling characteristics? (2) Despite the models' spreads, do the LSMs show common characteristics in L-A simulations and what might be the essential factors that contribute to them? To answer these questions, spatial patterns and annual variability of SMM from satellite estimations are first analyzed to provide a robust reference for multi-model assessments. Multi-model performances and influences of individual model's configurations including soil layer depths and coupling schemes are then evaluated. In order to diagnose possible reasons that may result in the models' biases, satellite-observed terrestrial water cycle parameters (i.e., precipitation stored in surface soil layer and ET at the water-limited stage) and soil moisture thresholds (i.e., soil wilting point θ_w and soil critical point θ_*) indicated from soil moisture memory are extracted and further compared with LSMs. The analyses provide satellite-based reference to diagnose L-A coupling characteristics in several prevailing LSMs, and provide readily available datasets to constrain the models' simulations at the global scale.

2 Materials and Methods

In this section, we will first give a brief review of basic concepts relevant to SMM. Explicit equations of the analyzed variables in this study are then given to address their physical indications.

SMM refers to the time between a perturbation starts and ceases in the time domain. Taking the wet scenario for example, when a perturbation occurs soil moisture loses water to the near-surface atmosphere through flux exchanges. The water loss persists with several sub-processes in order: (i) Drainage and runoff start to happen immediately after the precipitation when soil moisture is saturated; the two subprocesses cease when soil moisture is below the level when soil capillary is not able to hold water (field capacity, θ_{fc}); (ii) when soil moisture is below θ_{fc}, but is above a certain level (typically defined as the critical point, θ_c), the soil starts to evaporate at the maximum ET rate (also called Stage-I ET); (iii) When soil moisture is below θ_c, ET starts to happen at the water-limited rate (also named as Stage-II ET; the water-limited ET rate is typically determined by soil moisture content by first-order); (iv) the soil ceases to lose water when soil moisture is below soil wilting point θ_w. The entire loss can be defined as a function of soil moisture, i.e., Loss Function. The loss function can then be divided into two broad categories. When soil moisture is wet (i.e., above θ_c), the function is controlled by energy terms; otherwise, the function is limited by water conditions. The above processes can be described in Figure 1.

The energy-limited processes (i.e., drainage and stage-I ET) generally occur on timescales of hours to days. To identify these processes, soil moisture datasets with the comparable temporal resolution are required. Traditional SMM methods based on Markov processes (or other red-noise processes) were mostly developed based on soil moisture data with rather coarse temporal resolutions (e.g., monthly) due to data limitations. They generally combine the above physical processes at different stages. Therefore, the derived SMM only represents the overall L-A coupling strength without explicit physical indication. This impedes LSMs development since such L-A strength cannot be readily used for models' calibration.

The recently developed method based on a hybrid model instead characterizes SMM by considering energy- and water-limitations separately. The hybrid model is developed by using satellite soil moisture data with a temporal resolution of 3 days. Compared to traditional SMM results, the SMM at the energy- and water-limited stage can provide detailed references for calibration in LSMs, e.g., diagnosing which specific processes the L-A coupling biases come from. The hybrid model separates Loss Function by surface water conditions (i.e., the occurrence of precipitation events), and explicit equations for SMM at different regimes as well as relevant diagnoses are given in the following context.

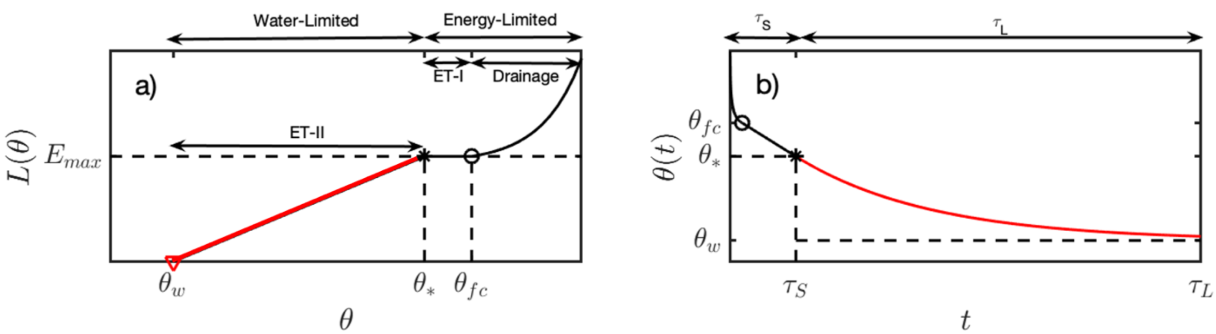

Figure 1 Schematic of surface water loss process (a) and soil moisture memory at different loss regimes (b). Figures are adapted from McColl et al. (2017b). Note that the *x-axis* in (a) refers to soil moisture (m^3 m^{-3}), and *y-axis* refers to surface water loss rate ($L(\theta)$, e.g., mm s^{-1}); E_{max} is the maximum evapotranspiration rate (the same unit as $L(\theta)$). While in (b), *x-axis* refers to time (e.g., days) and *y-axis* refers to soil moisture content (m^3 m^{-3}). θ_w, θ_*, and θ_{fc} refers to soil wilting point, critical point, and field capacity, respectively.

2.1 Soil moisture memory time at water-limited regime (τ_L) and energy-limited regime (τ_S)

Soil moisture memory in the water-limited regime (τ_L, L for the water-limited processes that usually occur at long time scales) and energy-limited regime (τ_S, S for the water-limited processes that usually occur at short time scales) are estimated from the hybrid model following McColl et al. (2019). The water-limited regime (i.e., Stage-II ET) is characterized by a deterministic equation since the processes at this stage usually occur in multi-days, a time scale that modern satellite measurements can characteristically resolve. Correspondingly, the water losses during the energy-limited stage often occur much more rapidly (e.g., hours to half a day).

In this case, a stochastic model is developed to describe a combination of unresolved processes (e.g., drainage, runoff and Stage-I ET). The hybrid model can be written as:

$$\frac{d\theta(t)}{dt} = \begin{cases} -\frac{\theta(t)-\theta_w}{\tau_L}, & P = 0 \\ -\frac{\theta(t)-\bar{\theta}}{\tau_S} + \varepsilon(t), & P > 0 \end{cases} \tag{1}$$

where, P refers to precipitation occurrence (a binary variable); θ is the volumetric soil moisture, and $\bar{\theta}$ refers to the time average soil moisture; ε is an independent random variable with a mean of zero; τ_L and τ_S refers to the soil moisture memory at the water-limited stage and energy-limited stage, respectively. Solving the above equations yields the explicit expressions of τ_L and τ_S, as:

$$\theta(t) = \begin{cases} \Delta\theta \exp\left(-\frac{t-\Delta t_P}{\tau_L}\right) + \theta_w, & P = 0 \quad (2a) \\ \overline{\theta(t-\Delta t_P)} + \frac{\alpha}{\Delta z} \exp\left(-\frac{\Delta t_P}{2\tau_S}\right), & P > 0 \quad (2b) \end{cases}$$

where, $\Delta\theta$ refers to the soil moisture change during each soil drying event; θ_w refers to the minimum soil moisture value; α is the precipitation intensity; Δz is the depth of surface soil layer, and $t = \Delta t_P$ refers to the time when the soil moisture drying starts to occur.

The energy-limited memory τ_S can then be calculated directly by rearranging the expression in (2b), as:

$$\tau_S = -\frac{\frac{\Delta t}{2}}{\log\left(\frac{\Delta z[\theta_+]}{\alpha}\right)} \tag{3}$$

where $[\theta_+] = \theta(t) - \overline{\theta(t-\Delta t)}$ refers to the positive increments of soil moisture; Δt refers to the temporal resolution of the input data.

However, since soil moisture is the only observation in (2a), and there are multiple unknowns (i.e., $\tau_L$and θ_w) to be parametrized, τ_L is then estimated by fitting the function to the soil moisture samples that are subject to water-limitation, namely, the drydown events. Drydown events here are identified as an event when the soil moisture changes are consistently negative. Additional rules including (1) θ_w is limited to be lower than the minimum value of the soil moisture time series; and (2) drydown events with less than 3 observation samples and events with $R^2 <$ 0.7 are filtered are applied to ensure credible fitting performance, consistent to McColl et al. (2017).

2.2 Terrestrial water cycle diagnostics informed from SMM

In addition to informing L-A coupling strength, another important role of soil memory is to provide relevant diagnostics of terrestrial water cycles. Specifically, the stored precipitation fraction F_p in τ_S provides an explicit estimation of how much precipitation can be retained by the surface soil layer. Therefore, it reflects the water-holding capacity of the soil. A decrease of F_p indicates the loss of soil water-holding capacity – thus more water will be stored in the near-surface atmosphere and induce the positive anomaly of rainfall and surface runoff (Liu et al., 2021). In this light, F_p can be viewed as a reasonable proxy for assessing flood risks in terrestrial water cycles. F_p can be described as the sum of positive soil moisture increments normalized by the total precipitation during a contemporary period and calculated as:

$$F_P(f) = \frac{\Delta z \sum_{i=1}^{fT} \Delta\theta_{i+}}{\int_0^T P(t)dt}, \tag{4}$$

where, f refers to the sampling frequency of the input data (d^{-1}) and T refers to the analyzed time period (days); Δz refers to soil layer depth (mm), $\Delta\theta_{i+}$ refers to positive soil moisture increments (m^3 m^{-3}); $\int_0^T P(t)dt$ is the accumulated precipitation (mm).

By using one-year SMAP soil moisture retrieval, McColl et al. (2017) has demonstrated a global median estimation of 0.14, that is, a thin 50mm soil layer (SMAP's nominal detecting depth) can retain approximately 14% of the precipitation falling on land. Subsequent studies have since referred to this amount as a benchmark to evaluate F_p in varying soil and climate conditions or how F_p will change in the future climate (Kim and Lakshmi, 2019; Liu et al., 2021; Martínez-Fernández et al., 2020). However, since soil moisture and precipitation both show annual variabilities, and the original SMAP products can contain larger noises compared to recent SMAP versions using an improved algorithm (e.g., Dual Channel Algorithm, MTDCA), it is necessary to examine the robustness of F_p distribution originally reported in McColl et al. (2017).

In terrestrial water cycles, ET is a core but difficult-to-estimate variable. Initially, gridded ET products have been developed to validate and improve simulations of soil moisture and other water-related variables in LSMs. At this phase, diverse ET products based on satellite estimations (Hu and Jia, 2015; Mu et al., 2014, 2007) and biophysical-constrained model datasets (Zhang et al., 2019; Zhao et al., 2019) have been developed, while most of them have shown moderate data accuracy compared to in-situ observations. However, few current ET products provide the ET information limited by surface water and energy availability, which plays an increasingly important role in the latest generation of LSMs. However, by integrating the surface water loss in the water-limited soil drying stage, the Stage-II ET can be readily estimated in this study to calibrate models' representations of surface water and energy variables. Annual accumulated Stage-II ET is calculated as:

$$ET_{II} = \sum_{i=1}^{n} \Delta z \theta_* (1 - \exp(\frac{\Delta dd_i}{\tau_L})) , \tag{5}$$

where, Δz is the soil layer depth (mm); θ_* refers to soil critical point (m^3 m^{-3}), Δdd_i refers to duration each drydown event persists (days), where n refers to the total soil moisture drydown number within the analyzed year, and i refers to the drydown event; τ_L indicates water-limited SMM (days).

2.3 Critical Soil moisture thresholds

Recall that soil moisture wilting point θ_w refers to the soil moisture level when ET ceases to occur, and the critical point θ_c refers to the soil moisture value that ET transforms from the energy-limited regime to water-limitation. In this case, the two thresholds correspond reasonably to the soil moisture values at both ends of the drydown events, i.e., θ_w and θ_c can be approximated by statistics (e.g., median or mean) of $\widehat{\theta_w}$ in (2b) and the initial soil moisture ($\widehat{\theta_p}$) at the beginning of each identified drydown event, when the total number of identified drydown events are statistically sufficient (e.g., more than 50 events within 5 years at each grid). We here use multi-year medians of $\widehat{\theta_w}$ and $\widehat{\theta_p}$ instead of their means because they represent the majority of the analyzed variables (as opposed to mean values that could be biased by extremes) (Feldman et al., 2021), although we acknowledge that theoretically the truth of θ_w and θ_* can hardly be obtained by using observations only.

We also note that the soil moisture thresholds retrieved from soil moisture time series may not facilitate direct comparisons with those encoded in LSMs, which are typically prescribed or calculated dependent on soil texture data (e.g., through Pedo-Transfer Functions, PTF hereafter). Therefore, we also compare $\widehat{\theta_w}$ and $\widehat{\theta_p}$ with the soil moisture thresholds calculated from the Global Soil Dataset for Earth System Modeling (GSDE, Shangguan et al., 2014), a soil texture dataset that is prevalently used in many LSMs (e.g., Noah LSM with Multiple Parameters, Noah-MP (Niu et al., 2011; Yang et al., 2011)). We use the PTF from Saxton and Rawls (2006) to include the organic matter effects. Additional PTF function from Clapp and Hornberger (1978) is also analyzed. Details of PTF function can be found in Supplementary Materials (Table S1).

3 Data

3.1 SMAP Surface Soil Moisture Data

Five annual cycles (i.e., April 1, 2015 to March 31, 2020) of soil moisture retrievals from Soil Moisture Active and Passive Mission (SMAP, (Entekhabi et al., 2010)) are used to obtain satellite estimation of τ_S and τ_L respectively. SMAP measures soil moisture at the surface soil layer (i.e., 0 – 5cm) from the L-band microwave radiometer. Validated by a large number of ground observations, SMAP SSM has been shown to have high accuracy to capture soil moisture timeseries compared to other microwave soil moisture products. SMAP has a nominal revisiting period of 3 days at the equator (1~2 days in polar regions), therefore it performs well in characterizing land-atmosphere coupling processes at weekly and sub-weekly time scales. Here we choose soil moisture products derived from the Multi-Temporal Dual Channel Algorithm (MTDCA) (Konings et al., 2016) since it uses time-invariant scattering albedo, and therefore reduces high-frequency noises. The spatial resolution of MTDCA product used in this study is 36km with EASE projections.

Prior to conducting the analysis, a quality control procedure has been applied to reduce the influences of noise encoded in satellite measurement. Consistent with several previous studies (McColl et al., 2019, 2017), soil moisture data over areas with dense vegetation cover (e.g., vegetation water content $\geq 5\ kg\ m^{-2}$), intense Radio Frequency Interference (RFI), water bodies, and frozen landscapes are filtered. In addition, since the surface water balance is easily affected by the temporal resolution of the analyzed SSM data, the SMAP soil moisture data are then resampled to a uniform sampling frequency of $1/3\ d^{-1}$ at each pixel (McColl et al., 2017).

3.2 Reanalysis Datasets

Surface soil moisture from six prevalent reanalysis datasets including Global Land Data Assimilation System v2.2 Catchment Land Surface Model (GLDAS-CLSM (Li et al., 2020)) and Global Land Data Assimilation System v2.1 Noah Model (GLDAS-Noah (Beaudoing, et al., 2020)) from Goddard Earth Science Data Information and Services Center (GES DISC) at the National Aeronautics and Space Administration (NASA), Modern-Era Retrospective Analysis for Research and Applications version2 (Merra2, (Gelaro et al., 2017)) from NASA's Global Modeling and Assimilation (GMAO), National Centers for Environmental Prediction Final Operational Global Analysis (NCEP-FNL, DOI: 10.5065/D6M043C6), European Center for Mesoscale Weather Forecast, version5 (ERA5(Hersbach et al., 2020)), and Japanese 55-year Reanalysis (JRA55, (Kobayashi et al., 2015)) from Japan Meteorological Agency are used to estimate soil moisture memory at different time scales.

All reanalysis datasets employed in this study are listed in Table 1. Among them, four distinctive LSMs, namely, the Catchment LSM, Noah LSM, (H)TSSEL and SiB are run with coupling scheme (to atmosphere model) to produce soil moisture simulations for MERRA2, NCEP, ERA5 and JRA55, respectively. Comparing soil memory analysis between these datasets could inform the model-dependent L-A coupling characteristics (e.g., consistency and divergence of LSMs' performance in L-A interactions). Two LSMs (i.e., Catchment and Noah LSMs) are run with offline coupling scheme to provide soil moisture data for GLDAS-Catchment and GLDAS-Noah. Comparing results from these two datasets with analyses from other LSMs can diagnose the effects of atmospheric processes (e.g., moist convection and turbulence mixing) on L-A interactions. We note that the soil layer depth is 10 cm in all datasets in this study, except for the GLDAS-CLSM and JRA55, which has a topsoil layer of 2cm. Comparing memory results estimated from these two models with others could inform the influence of soil depths on flux exchanges at the land-atmosphere interface. All the soil moisture data are aggregated to a common

36 km spatial resolution, and their temporal resolutions are resampled to 1/3 day^{-1}, consistent to SMAP observations.

Table 1. Detailed information of six reanalysis datasets in this study

Data Names	LSMs	Surface Soil Layer Depth	Spatial Resolution	Temporal Resolution
GLDAS-CLSMv2.2	Catchment (offline)	0-2cm	0.25° ×0.25°	1 day
GLDAS-Noahv2.1	Noah (offline)	0-10cm	0.25° ×0.25°	3 hours
MERRA2	Catchment (coupled)	0-10cm	0.625° ×0.5°	1hour
NCEP	Noah (coupled)	0-10cm	1° ×1°	6 hours
ERA5	(H)TESSEL (coupled)	0-10cm	0.25° ×0.25°	1 hour
JRA55*	SiB (coupled)	0-2cm	0.5° ×0.5°	3hours

3.3 GPM Precipitation Data

Precipitation information is needed when calculating soil memory in the energy-limited regime (τ_S). Here, we use Late-Run Integrated Multi-Satellite Retrievals (IMERG) from NASA's Global Precipitation Mission (GPM) (Huffman et al., 2019). The IMERG product has a spatial resolution of 0.1°, and is regridded to 36km. The half-hourly data are then converted from UTC to daily 6 a.m. local time to be consistent with SMAP's overpass time. Similar to (McColl et al., 2019), the satellite-observed precipitation data, rather than the precipitation forcing that drives

LSMs, are used when estimating τ_S for the reanalysis datasets to isolate the impact of soil moisture on the comparison between observations and models.

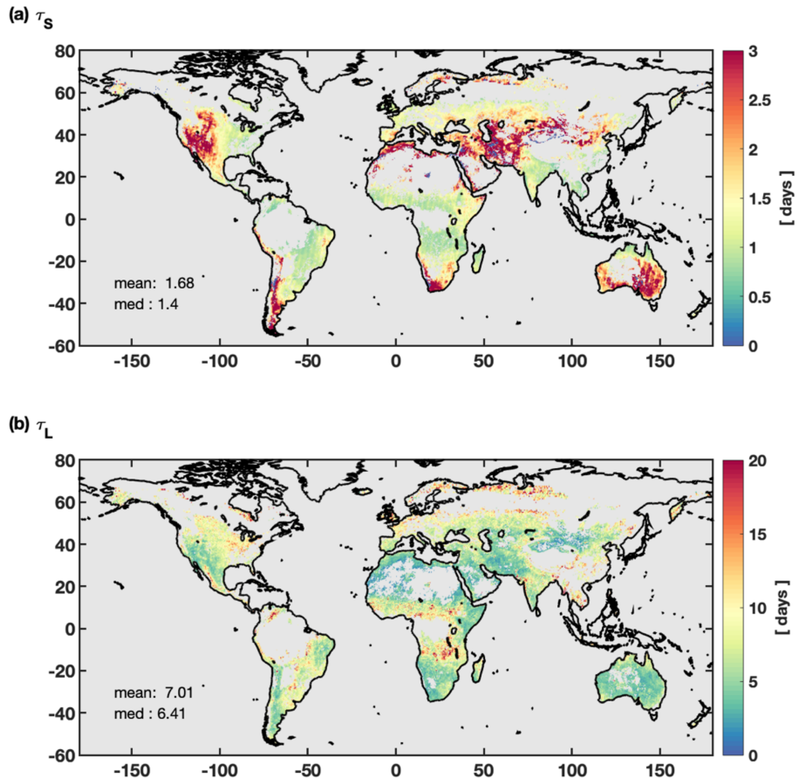

Figure 2 Global distribution of energy-limited soil moisture memory (τ_S, (a)) and water-limited memory (τ_L, (b)) estimated from 5-year SMAP datasets. Inserted texts refer to global mean and median values.

4 Results

4.1 τ_S and τ_L estimated from SMAP SSM data

Figure 2 shows the global distribution of median τ_L and τ_S estimated from 5-yr SMAP observations. At the global scale, the energy-limited soil memory time τ_S is longer over arid regions (such as the Midwest of the United States and central Australia) whereas the water-limited soil memory time τ_L is longer over wet areas, corresponding reasonably to the spatial distribution of soil hydraulic properties – the wet areas tend to have higher soil hydraulic conductivity thus precipitation drains more rapidly into the deep soils. The Spearman's correlation ($\rho = 0.51, p < 0.05$) further suggests these two memory scales are spatially anti-correlated (Figure S1), which compare consistently to analyses reported in previous studies (McColl et al., 2017b, 2019).

In addition to the spatial pattern, we also analyze the temporal variability of τ_L and τ_S, which has not yet gained particular concern in literature. We emphasize that the soil memory time discussed in this study are two proxies for measuring L-A coupling strength, therefore their temporal variability (e.g., year-to-year variations) may significantly change the spatial pattern and frequency of the occurrences of extreme events. Figure 3 shows that annual variations of the soil memory time within the study period (i.e., 2015-2019). Results show that both τ_L and τ_S remain consistently unchanged within a rather long-term. Although the τ_L shows the longer-tailed distribution in the year 2019, the low density of τ_L with "extreme" values indicates this does not influence the overall distribution. These results indicate that the spatial pattern of different soil drying regimes remains qualitatively fixed and the drying rates do not change over time. Moreover, these results also suggest that the satellite estimates of τ_L and τ_S are robust and can serve as credible references to examine the L-A coupling strength in the reanalysis datasets.

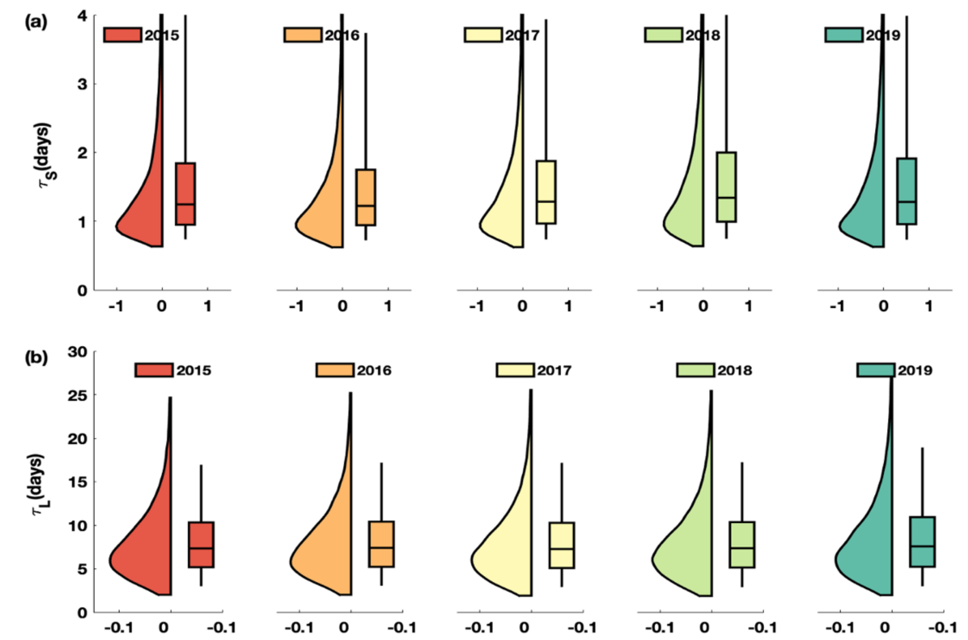

Figure 3 Annual variability of statistics for τ_S (above) and τ_L (below) estimated from SMAP observation. Polygons indicate Probability Density (PDF) curves.

4.2 τ_S and τ_L from reanalysis data

Figure 4 shows the scatterplots of the multi-model mean of τ_L and τ_S estimates, and their comparison with the SMAP observations, respectively. The global maps of multi-model means are shown in Figure S2 of the supplementary material. The results show that current LSMs can present reasonable anti-correlated patterns of τ_L and τ_S with Spearman's correlation of -0.37. The global multi-model mean maps also show that τ_S is longer in arid areas while long τ_L occurs in wet areas (Figure S2). However, by comparing τ_L and τ_S with satellite estimates, respectively, Figure 4a and Figure 4b show that the energy-limited soil memory is underestimated while the memory time at the water-limited regime is overestimated, indicating that L-A processes at different time scales are generally misrepresented by LSMs.

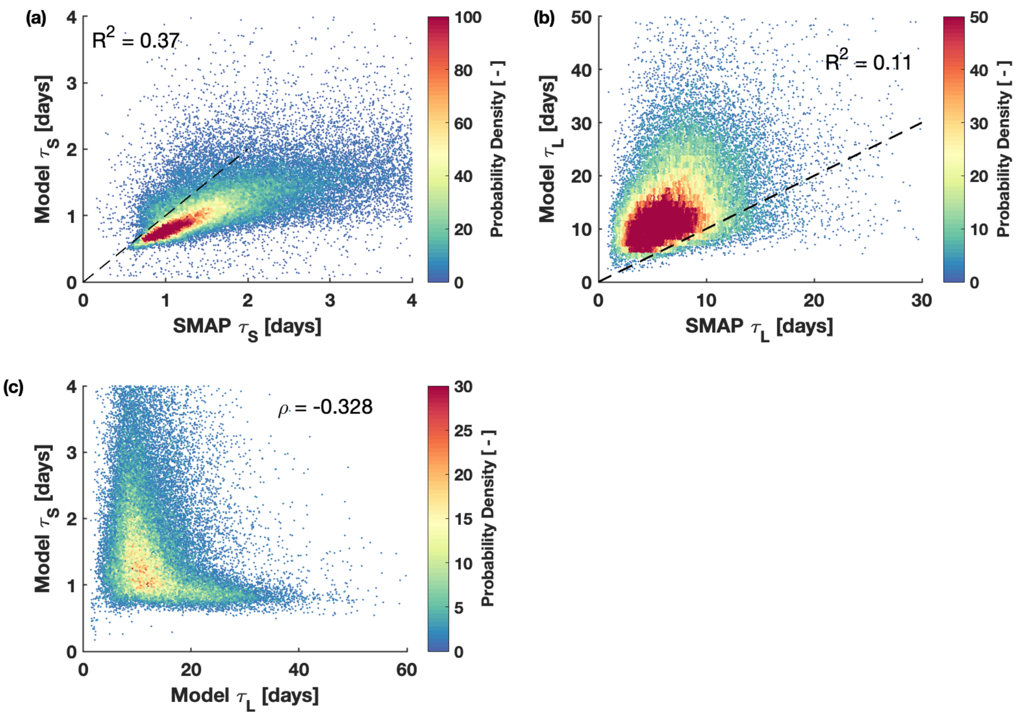

Figure 4 Scatterplots of multi-model mean of τ_S (a) and τ_L (b) versus SMAP estimation. (c) refer to the scatterplot between τ_S versus τ_L. Inserted texts are correlations between each pair of the analyzed variables. Colorbars indicates probability density.

There could be multiple reasons (e.g., model's physical parameterizations, coupling schemes, etc.) that can lead to memory biases in current LSMs. Individual models may thus perform strong disagreement in capturing L-A characteristics. Figure 5 and Figure 6 show the inter-comparison of τ_L and τ_S between six reanalysis datasets as well as SMAP observations, respectively. Consistent to the multi-model mean results, the six analyzed datasets all show substantial underestimations of τ_S and overestimation of τ_L compared to satellite estimates. However, the biases in model-estimated memory time show large model spreads. Specifically, GLDAS-CLSM and JRA55 present the two largest underestimations for the energy-limited memory time, with a median of 0.57 and 0.7 day compared to 1.4 days of SMAP estimates, respectively. The other four datasets show similar underestimations (Figure 5, b - e) of the τ_S results; however, the τ_S estimations of these four datasets compare more closely to SMAP, relevant to GLDAS-CLSM and JRA55. This could be relevant to soil depth. The topsoil depth prescribed in GLDAS-CLSM and JRA55 is 2cm, only one-fifth of those in other LSMs. Since τ_S reflects the soil water-holding capacity and is a direct function of soil layer thickness, it is not strange that a model with a thinner soil layer would exhibit more rapid drainage or ET-I drying rates. However, for the other models such as GLDAS-Noah, MERRA2, NCEP-FNL and ERA5, in which the soil depths are twice as much as the nominal detecting depth of SMAP, τ_S estimates are still underestimated with medians around 0.3 day.

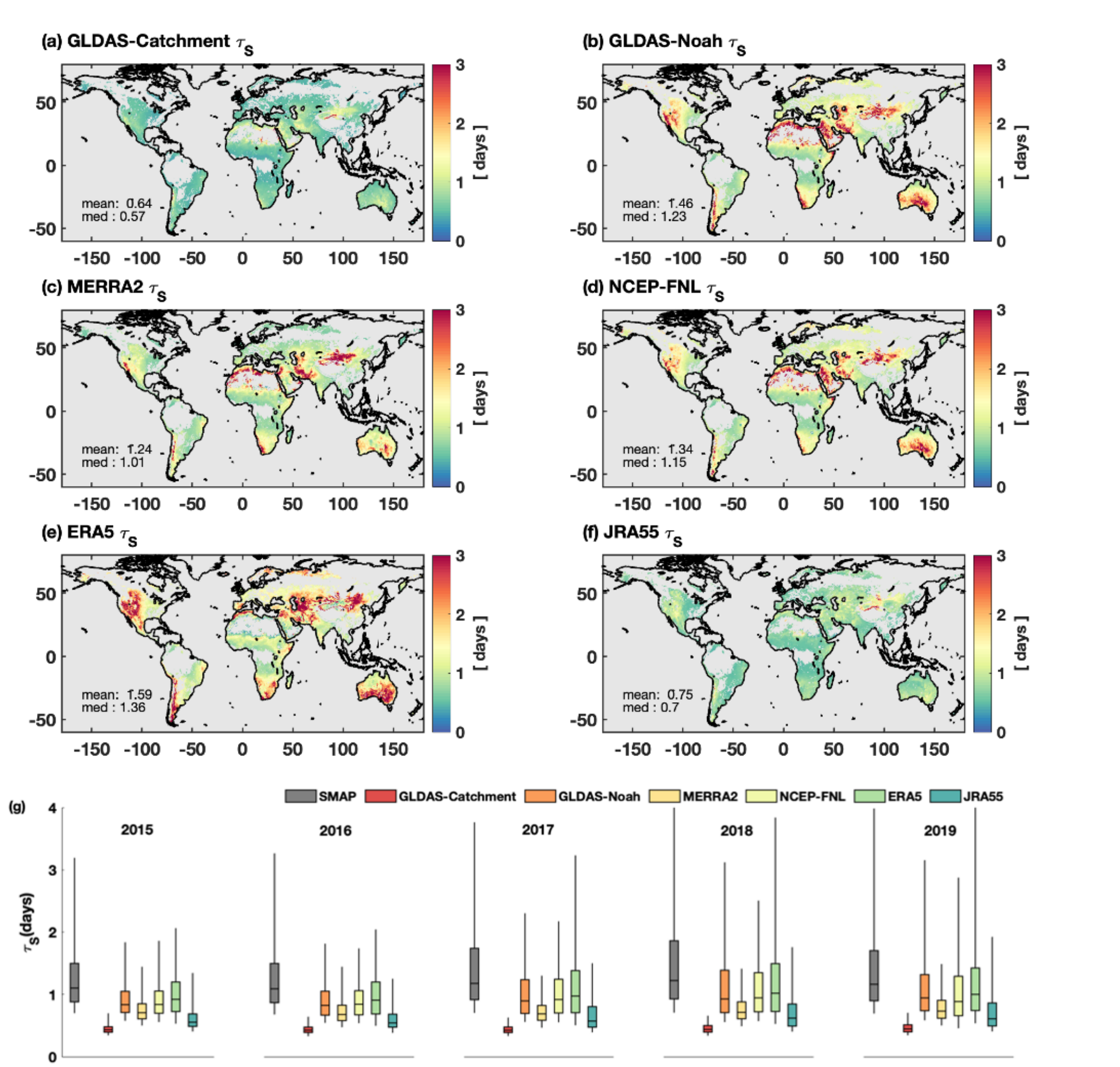

Figure 5 Global distribution of τ_S for each individual model (a – f) and the annual variability of their statistics (g). Inserted texts in (a – f) refer to global mean and median values for each model.

Compared to τ_S results, the models show an overall overestimation of τ_L. In contrast to τ_S results, the model estimated τ_L also shows a large model spread but the inter-model comparison does not show high relevance to soil layer thickness. This may indicate that the water-limited processes, in particular, the stage-II ET process at the surface soil layer is more tightly related to deeper soils than the energy-limited processes such as drainage and runoff. The largest τ_L median overestimation is presented by MERRA2 instead of GLDAS-CLSM. Moderate τ_L biases are presented in GLDAS-Noah, NCEP-FNL and ERA5, with their medians more than twice as compared to SMAP observations. τ_L estimation from JRA55 shows to be the closest to SMAP estimate, verifying that the parameterizations in SiB LSM perform better in the characterizations of water-limited soil drying processes.

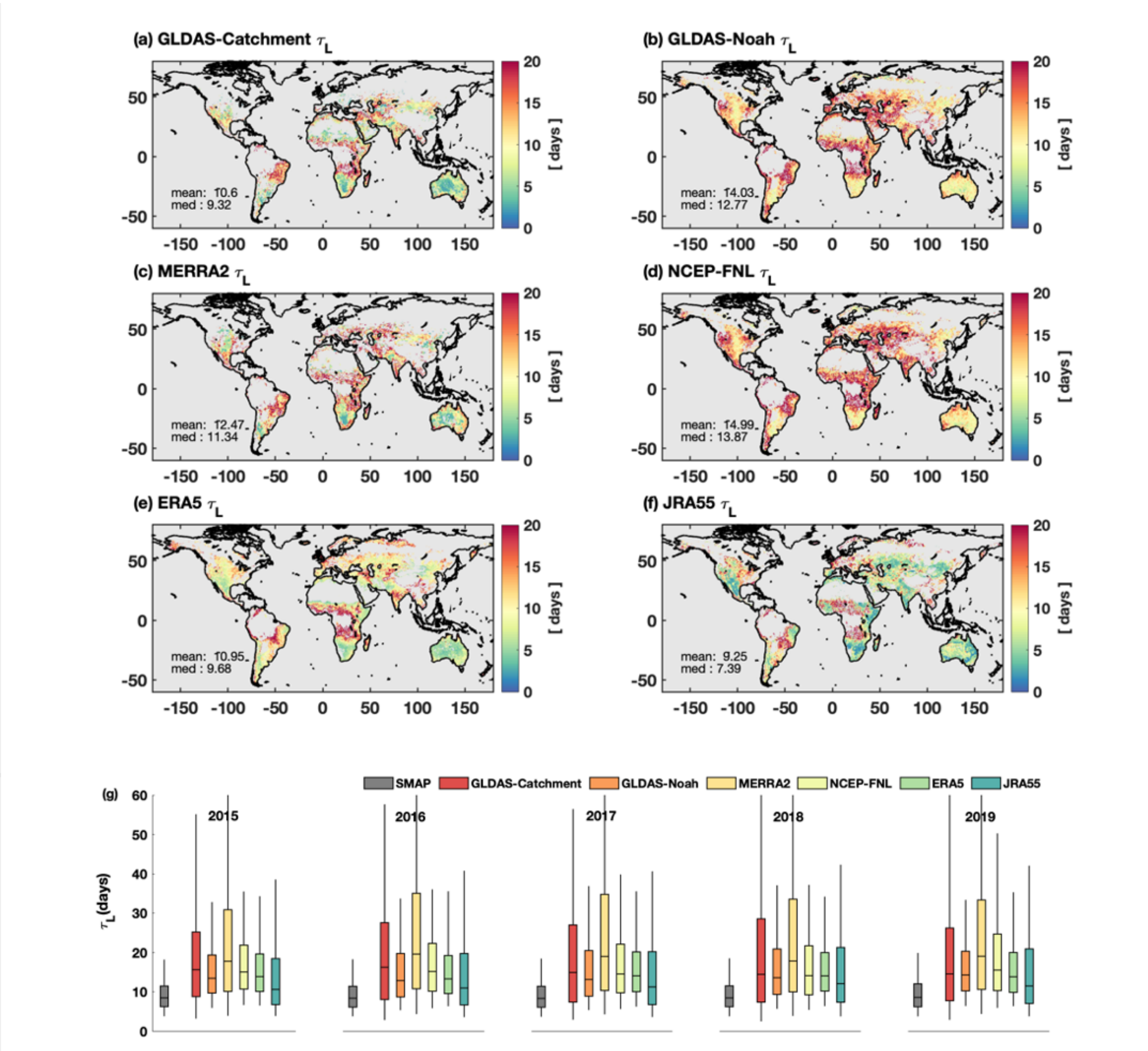

Figure 6 Same as Figure 5 **Global distribution of τ_S for each individual model (a – f) and the annual variability of their statistics (g). Inserted texts in (a – f) refer to global mean and median values for each model.**but for τ_L.

In addition to the model dependence and soil layer depth, we also find that neither τ_S nor τ_L estimate is highly sensitive to the models' coupling schemes. For example, for GLDAS-Noah and NCEP-FNL, both of which use Noah LSM but are run with different coupling schemes, e.g., the LSM is run offline in GLDAS-Noah while is coupled to the atmospheric model in NCEP-FNL, τ_S and τ_L both show similar statistics (e.g., medians, quantiles and ranges). While the memory results in the other pair (i.e., GLDAS-Catchment and MERRA2) show relatively larger differences, this discrepancy can be possibly attributed to the model's inconsistencies in soil layer thickness. By comparison, previous studies have shown that land properties (i.e., soil organic matter) can have different effects on surface states (e.g., soil temperature and near-surface air temperature) in coupled and uncoupled LSMs, respectively (citations, Sun et al., 202?). However, we note that these analyses only focus on surface state variables rather than diagnostics related to time-variant processes. Our results, by analyzing the soil drying time, show that the atmospheric processes play minor roles in regulating land surface processes at time scales of hours to subweekly. The above analyses suggest that the underestimation of SMM in current LSMs is not caused by soil layer depths or the models' online/offline simulating schemes, but by other factors such as the models' employment of physical parametrizations and static parameters (such as soil and vegetation properties).

4.3 Terrestrial water cycle diagnostics informed by τ_S and τ_L

Figure 7 shows the comparison of F_p (left column) and Stage-II ET (right column) estimation between multi-model mean and satellite-based estimations. Only four datasets with equal soil layer depth (10 cm) are chosen here to represent the majority of the analyzed models since ET is accumulated with soil layer depths. Results including GLDAS-CLSM and JRA55 are shown in Figure S3 in the supplementary materials.

F_p estimate based on five-year SMAP SSM retrievals presents a similar global pattern, but with a median of 23% compared to 14.4% reported in McColl et al (2017). Since F_p is essentially relevant to "wet" risks (e.g., floods) at synoptic time scales (Liu et al., 2021), a 7% difference in F_p may result in a different global pattern of water-related extreme events. This means the comparison of F_p between the original SMAP soil moisture estimation and results from other remote sensing products and climate models should be further validated. For example, Liu et al. (2021) show that one current LSM (i.e., CLM) produces consistent F_p to satellite estimation. Therefore, they use historical simulations from CLM as a baseline to compare with F_p projections in future climate, and conclude that the precipitation retained in the surface soil layer could possibly decrease. However, the multi-model mean estimate from four reanalysis datasets suggests that current LSMs present an underestimation of F_p evaluated by both mean (21% of models vs. 28% of satellite) and median (18% of models vs. 23% of satellite) statistics. Results including all datasets lead to a consistent conclusion. This result indicates that assessments of future F_p projections may be re-examined with the historical reference redefined.

The annual Stage-II ET from a five-year SMAP estimation presents a global median of 47.91 mm yr^{-1}, showing several hotspots (e.g., Stage-II ET > 100 mm yr^{-1}) occurring in the central US, South America, and eastern Australia. By comparison, the multi-model mean (of four analyzed datasets) shows an underestimation of Stage-II ET with a global median of 39.67 mm yr^{-1}. Stage-II ET of six-model-mean is even lower, with a global median of only 35.75 mm yr^{-1}. Particularly, Stage-II ET hotspots (including the central US, which has previously been identified as one of the regions that have the strongest L-A coupling strength on the globe by Koster et al. (2004)) are muted in the multi-model mean results. The above results suggest that the flood risks are underestimated in current LSMs, and the observed water-limitations on Stage-II ET are more severe than characterized in models. As such, calibrating models' surface energy partitioning processes (e.g., soil moisture and ET coupling regimes) with observed evidence may help to improve models' representations of L-A interactions.

The F_p results show consistent model spread to Stage-II ET results as well as spread in energy-limited soil moisture memory τ_S (Figure S4 and Figure S5). Still, the results are highly sensitive to soil depth and models' parameterization schemes, but show insignificant sensitivity to models' coupling schemes. For example, both F_p and Stage-II ET from GLDAS-CLSM and JRA55 are much lower than other models due to the soil depth configuration, and the differences between ERA5 and other models with consistent soil depth (i.e., GLDAS-Noah, MERRA2 and NCEP-FNL) are more distinctive than those between models with different coupling schemes (e.g., MERRA2 and NCEP-FNL).

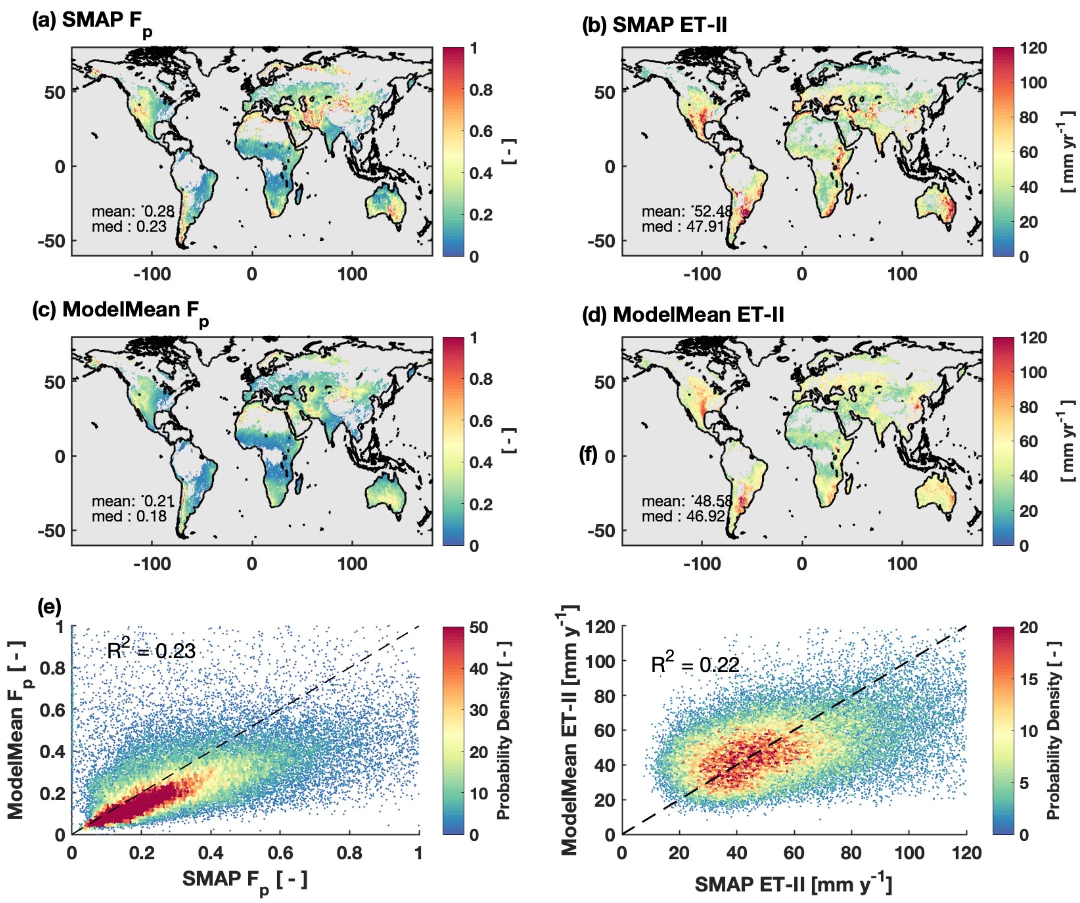

Figure 7 Global distribution of precipitation fraction (F_p, left column) and stage-II ET (right column) for multi-model mean (a – d), and their scatterplot versus SMAP estimations. Since ET is accumulated with soil layer depths, only four models with 10 cm soil layers are shown here. Results of including all models are shown in Figure S3.

4.4 Critical soil moisture thresholds

The above results suggest that current LSMs' biases in L-A simulation are highly dependent on the models' parameterizations (including the physical schemes and the models' static parameters). However, systematically evaluating the effects of the models' physical schemes on the L-A coupling biases could be highly labor-intensive and time-consuming. Therefore, we chose to first evaluate one core component of the LSMs' static parameters, the soil hydraulic thresholds because of their high relevance to SMM, to explore the essential factors that might contribute to the models' L-A simulating biases.

Figure 8a and Figure 8c show the comparison of global soil wilting point θ_w between SMAP observation and multi-model mean. The results show an overall similar global pattern, with θ_w higher in strong L-A coupling hotspots. However, the SMAP observed θ_w shows much less spatial heterogeneity, e.g., it has a narrower range (except for the hotspots, θ_w in most areas are between 0.04 m^3 m^{-3} and 0.06 m^3 m^{-3}). Comparison between the multi-model mean and the SMAP observation shows that the models present a substantial overestimation of θ_w – the multi-model mean shows a global median of 0.13 m^3 m^{-3} versus 0.05 m^3 m^{-3} of SMAP. The scatterplot further validates the conclusion (Figure 8e). Similar overestimation is also observed in models' soil moisture critical point θ_c (Figure 8b and Figure 8d). The global median θ_c of satellite-estimated and multi-model mean are 0.24 m^3 m^{-3} and 0.27 m^3 m^{-3} respectively. In contrast to θ_w, the multi-model mean of θ_c shows a particularly large overestimation in the strong L-A coupling areas.

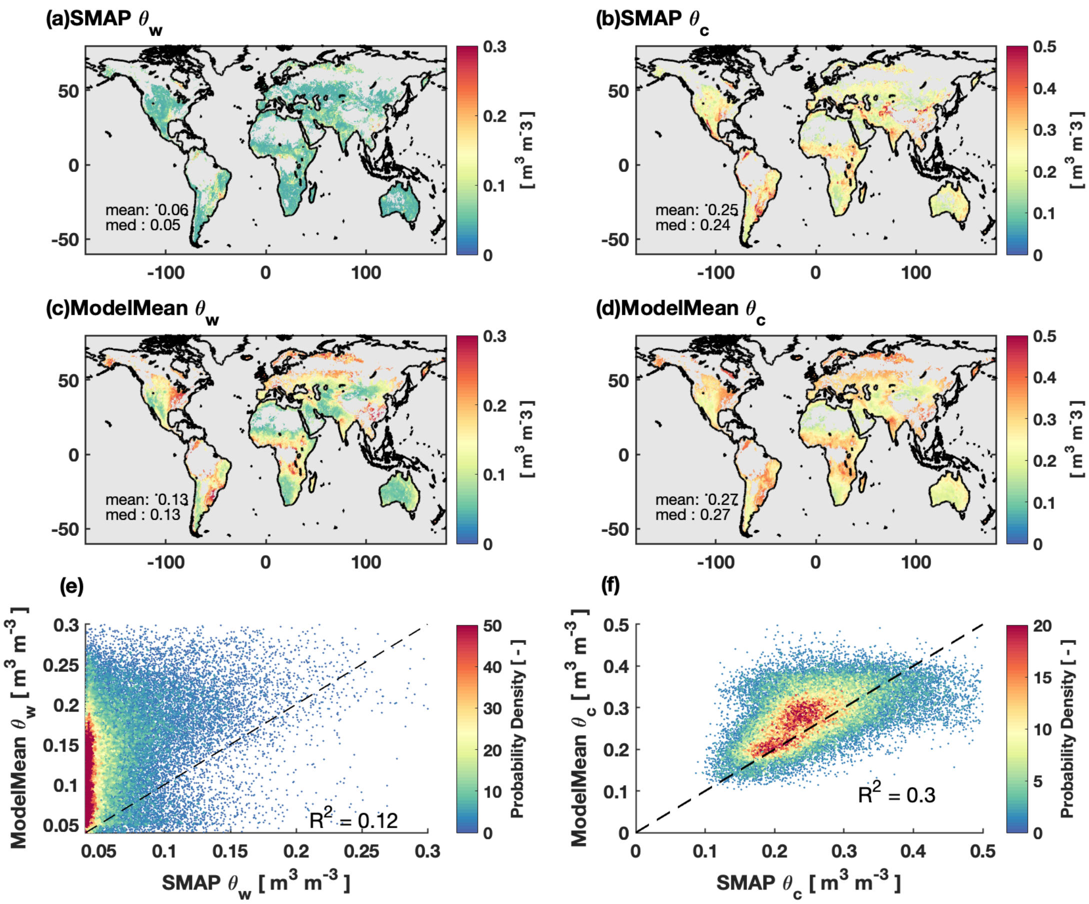

Figure 8 Global distribution of soil wilting point (θ_w, left column) and critical point (θ_c, right column) for multi-model mean (a – d), and their scatterplot versus SMAP estimations. Areas where $\theta_w < 0.04$ m^3 m^{-3} are masked to mitigate noises induced by data quality.

Figure 9 shows the intercomparison of model spreads as well as the annual variability of θ_w and θ_c. Overall, the soil moisture thresholds estimated from models and satellite observation are robust within the five annual cycles. θ_w and θ_c of the models compare consistently overestimated to the SMAP observations. Intercomparison between individual models further shows that in contrast to soil memory and water cycle diagnostics, the soil moisture thresholds show minor sensitivity to models' soil layer depth or parameterization schemes. This indicates that the LSMs' L-A simulating biases may be commonly dominated by misrepresentations of soil hydraulic characteristics.

We note again the θ_w and θ_c retrieved from models' SM time series are not exactly the one that drives LSMs – soil parameters are often calculated from soil texture data in LSMs. Therefore, we compare the soil texture-based thresholds in order to diagnose possible reasons that may be responsible for uncertainties in models' L-A presentations. Figures S6-S7 show the global distribution of soil moisture thresholds calculated from GSDE soil texture data. The texture-based

θ_w and θ_c compare similarly to the thresholds retrieved from models' soil moisture timeseries and show consistent differences to the SMAP estimations. Comparison with thresholds calculated from Clapp and Hornberger (1978) scheme results in a consistent conclusion (Figure S8-S9). The similarity between retrieved- and texture-based results and their differences from satellite estimations suggest that the soil moisture thresholds could be highly relevant to the models' L-A coupling simulations, especially for simulations related to the energy-limited processes. Therefore, calibrating the soil texture datasets based on large-scale observational soil hydraulic thresholds may provide an efficient approach to improve the models' performances in L-A coupling simulations.

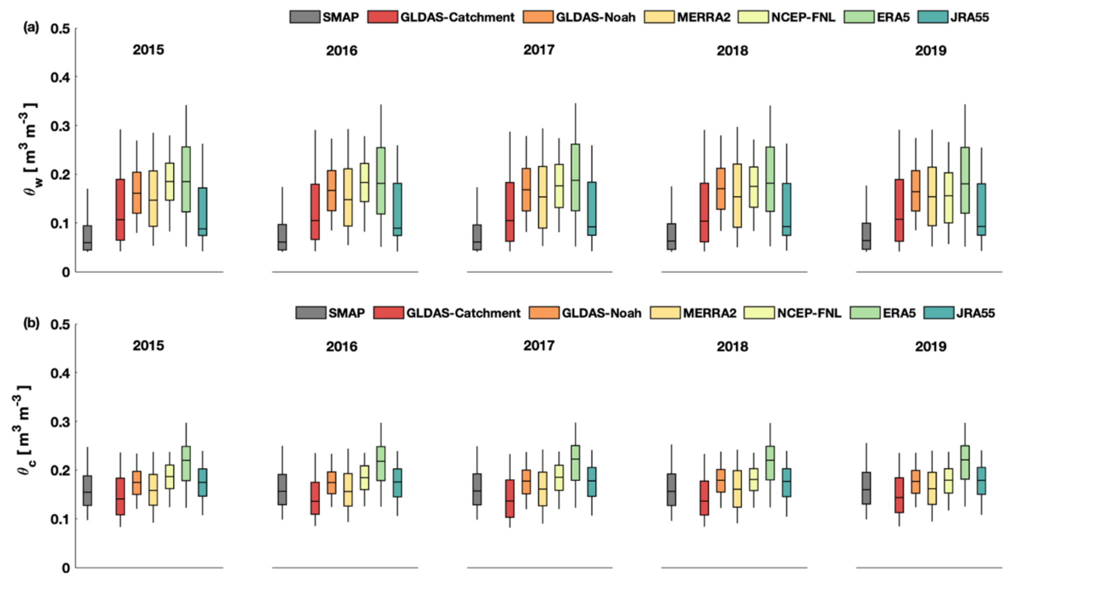

Figure 9 Annual variability of statistics for θ_w (above) and θ_c (below) of each individual models.

5 Conclusions

This study provides global evaluations of surface soil memory in six prevalently-used reanalysis datasets by using multi-year satellite estimations. The results show that the multi-model mean presents an overestimation of water-limited soil memory τ_L whereas tends to underestimate the energy-limited soil memory τ_S, suggesting that the soil memory biases reported previously in one or two example model(s) are prevalent in current LSMs. Large model spreads are observed between individual models, where the soil memory biases are highly dependent on models' parameterizations such as the static soil hydraulic property data, while showing minor relevance to the models' soil layer depth or online/offline simulating schemes.

Our study also provides a satellite-based estimation of two important terrestrial water cycle-related variables (i.e., the precipitation fraction F_p for assessing flood risks and water-limited evapotranspiration ET-II) at the global scale. The five-year mean F_p presents a 7% increase (i.e., the newly estimated F_p is 23%) in the global median to the originally reported results, indicating moderate sensitivity of observed flood risks to the remote sensing products. This also suggests that future assessments of F_p, as well as flood risks in climate models, should consider factors such as the robustness of the reference F_p datasets. The satellite estimation of ET-II shows reasonable spatial distribution compared to the observed pattern of strong L-A coupling regions. Compared to prevailing ET products, the advantage of ET-II in our study is that we separate ET limited by surface water availability from the ET partitioning processes with explicit physical meaning. As ET partitioning regulates carbon redistribution of plants, and energy and water exchanges between land and near-surface atmosphere (Akbar et al., 2019; Feldman et al., 2020, 2019; Williams and Torn, 2015; Zhou et al., 2016), calibrating the physical parameterizations such as surface resistance or carbon assimilation schemes with satellite-observed Stage-II ET may improve the simulations of L-A coupling variables (e.g., soil moisture and temperature) and vegetation dynamics (e.g., Gross Primary Production, Transpiration-ET ratio) in LSMs.

Global satellite-based soil hydraulic parameters (i.e., the soil moisture wilting point θ_w and critical point θ_c) are finally provided. The θ_w and θ_c statistics are robust within five annual cycles. The multi-model results show substantial differences in both θ_w and θ_c from the satellite estimates. Comparison with texture-based analysis confirms the conclusion. Large-scale products of soil hydraulic parameters are typically provided by extrapolating in-situ measurements from geographical survey records, where the data quality is only vaguely defined (Bouma, 1989; Dai et al., 2019). Our study, by comparing global observational evidence, further shows that the texture-based estimations of θ_w and θ_c are both overestimated. Furthermore, the soil hydraulic parameters are directly related to soil texture. As such, the results indicate the soil texture information may be improved by optimizing from satellite-observed θ_w and θ_c, and thus could enable considerable improvements of the equilibrium soil moisture simulation biases in many LSMs.

Several limitations, however, should also be addressed in this study. ET-II and soil moisture thresholds θ_w and θ_c are both estimated by characterizing soil moisture drydown curves. The method itself contains uncertainty. For example, when fitting the drydown timeseries, the functional forms, e.g., using the logarithmic function instead of the exponential function, may lead to different estimations. However, updating the fitting function would need additional hypotheses and may bring in extra uncertainty, and the derivation of a new method to characterize the drydown processes is beyond the scope of this study. The parameter boundaries (e.g., the minimum soil moisture values, and upper and lower boundary limits of constants in the fitting procedure) would also lead to different results. However, we have tested the fitting procedure by changing boundary limits, and the results show that the influence on parameters is minor (not shown).

Another factor that may affect the results is the soil moisture sampling frequency. The sampling frequency used in this study is 1/3 d^{-1}(reverse of SMAP's nominal revisiting period), therefore different estimations of soil memory as well as relevant diagnostics should be expected when land processes occurred within 3 days are included. In addition, 5-year soil moisture data may still be insufficient to produce a robust estimate of these variables. Sensitivity of ET-II and soil moisture thresholds to these factors are thus expected by using soil moisture datasets with higher sampling frequency and long temporal coverage available (e.g., a recently developed soil moisture datasets from the neural network (Yao et al., 2021) provides daily satellite-based soil moisture products with 20-year temporal coverage). However, we emphasize that the primary aim of this study is to provide evaluations of L-A coupling performance in several prevalently-used reanalysis datasets with satellite-observed evidence. However, since credible L-A products are essentially important for improvements in current LSMs, future practices are heartily expected to produce such datasets with high and robust data quality.

Acknowledgments

This study is supported by the National Key Research and Development Program of China (2017YFA0603703), the Second Tibetan Plateau Scientific Expedition and Research Program (STEP, grant No. 2019QZKK0206), and the International Parternership Program of Chinese Academy of Sciences (182211KYSB20200015). We thank Andrew Feldman for providing the MTDCA soil moisture data.

Open Research

SMAP soil moisture data are available at https://doi.org/10.6084/m9.figshare.21184366.v1 ; GLDAS-CLSMv2.2 datasets are available from https://disc.gsfc.nasa.gov/datasets/GLDAS_CLSM025_DA1_D_2.2/summary?keywords=GLDAS . GLDAS-Noah data are available from https://disc.gsfc.nasa.gov/datasets/GLDAS_NOAH025_3H_2.1/summary?keywords=GLDAS ; MERRA2 is available from https://disc.gsfc.nasa.gov/datasets/M2T1NXLND_5.12.4/summary ; NCEP-FNL is available from https://rda.ucar.edu/datasets/ds083.2/ ; ERA5 is available from https://cds.climate.copernicus.eu/cdsapp#!/dataset/reanalysis-era5-single-levels?tab=overview ; JRA55 is available from https://rda.ucar.edu/datasets/ds628.0/ ; GPM precipitation data is available from https://gpm1.gesdisc.eosdis.nasa.gov/data/GPM_L3/GPM_3IMERGHH.06/ ; GSDE soil texture data is available from http://globalchange.bnu.edu.cn/research/soilw .

References

Akbar, R., Short Gianotti, D.J., Salvucci, G.D., Entekhabi, D., 2019. Mapped Hydroclimatology of Evapotranspiration and Drainage Runoff Using SMAP Brightness Temperature

Observations and Precipitation Information. Water Resour. Res. 55, 3391–3413. https://doi.org/10.1029/2018WR024459
Beaudoing, H., Rodell, M., NASA/GSFC/HSL, 2020. GLDAS Noah Land Surface Model L4 3 hourly 0.25 x 0.25 degree, Version 2.1. https://doi.org/10.5067/E7TYRXPJKWOQ
Berg, A., Sheffield, J., 2018. Soil Moisture–Evapotranspiration Coupling in CMIP5 Models: Relationship with Simulated Climate and Projections. Journal of Climate 31, 4865–4878. https://doi.org/10.1175/JCLI-D-17-0757.1
Bouma, J., 1989. Using Soil Survey Data for Quantitative Land Evaluation, in: Lal, R., Stewart, B.A. (Eds.), Soil Restoration, Advances in Soil Science. Springer New York, New York, NY, pp. 177–213. https://doi.org/10.1007/978-1-4612-3532-3_4
Clapp, R.B., Hornberger, G.M., 1978. Empirical equations for some soil hydraulic properties. Water Resour. Res. 14, 601–604. https://doi.org/10.1029/WR014i004p00601
Dai, Y., Shangguan, W., Wei, N., Xin, Q., Yuan, H., Zhang, S., Liu, S., Lu, X., Wang, D., Yan, F., 2019. A review of the global soil property maps for Earth system models. SOIL 5, 137–158. https://doi.org/10.5194/soil-5-137-2019
Delworth, T.L., Manabe, S., 1988. The Influence of Potential Evaporation on the Variabilities of Simulated Soil Wetness and Climate. J. Climate 1, 523–547.
Dirmeyer, P.A., 2011. The terrestrial segment of soil moisture-climate coupling: SOIL MOISTURE-CLIMATE COUPLING. Geophysical Research Letters 38, n/a-n/a. https://doi.org/10.1029/2011GL048268
Dirmeyer, P.A., Koster, R.D., Guo, Z., 2006. Do Global Models Properly Represent the Feedback between Land and Atmosphere? J. Hydrometeor 7, 1177–1198. https://doi.org/10.1175/JHM532.1
Dirmeyer, P.A., Schlosser, C.A., Brubaker, K.L., 2009. Precipitation, Recycling, and Land Memory: An Integrated Analysis. Journal of Hydrometeorology 10, 278–288. https://doi.org/10.1175/2008JHM1016.1
Entekhabi, D., Njoku, E.G., O'Neill, P.E., Kellogg, K.H., Crow, W.T., Edelstein, W.N., Entin, J.K., Goodman, S.D., Jackson, T.J., Johnson, J., Kimball, J., Piepmeier, J.R., Koster, R.D., Martin, N., McDonald, K.C., Moghaddam, M., Moran, S., Reichle, R., Shi, J.C., Spencer, M.W., Thurman, S.W., Tsang, L., Van Zyl, J., 2010. The Soil Moisture Active Passive (SMAP) Mission. Proc. IEEE 98, 704–716. https://doi.org/10.1109/JPROC.2010.2043918
Feldman, A.F., Short Gianotti, D.J., Konings, A.G., Gentine, P., Entekhabi, D., 2021. Patterns of plant rehydration and growth following pulses of soil moisture availability. Biogeosciences 18, 831–847. https://doi.org/10.5194/bg-18-831-2021
Feldman, A.F., Short Gianotti, D.J., Trigo, I.F., Salvucci, G.D., Entekhabi, D., 2020. Land-Atmosphere Drivers of Landscape-Scale Plant Water Content Loss. Geophys. Res. Lett. 47. https://doi.org/10.1029/2020GL090331
Feldman, A.F., Short Gianotti, D.J., Trigo, I.F., Salvucci, G.D., Entekhabi, D., 2019. Satellite-Based Assessment of Land Surface Energy Partitioning–Soil Moisture Relationships and Effects of Confounding Variables. Water Resour. Res. 55, 10657–10677. https://doi.org/10.1029/2019WR025874
Gallego-Elvira, B., Taylor, C.M., Harris, P.P., Ghent, D., Veal, K.L., Folwell, S.S., 2016. Global observational diagnosis of soil moisture control on the land surface energy balance. Geophys. Res. Lett. 43, 2623–2631. https://doi.org/10.1002/2016GL068178

Gelaro, R., McCarty, W., Suárez, M.J., Todling, R., Molod, A., Takacs, L., Randles, C.A., Darmenov, A., Bosilovich, M.G., Reichle, R., Wargan, K., Coy, L., Cullather, R., Draper, C., Akella, S., Buchard, V., Conaty, A., da Silva, A.M., Gu, W., Kim, G.-K., Koster, R., Lucchesi, R., Merkova, D., Nielsen, J.E., Partyka, G., Pawson, S., Putman, W., Rienecker, M., Schubert, S.D., Sienkiewicz, M., Zhao, B., 2017. The Modern-Era Retrospective Analysis for Research and Applications, Version 2 (MERRA-2). J. Climate 30, 5419–5454. https://doi.org/10.1175/JCLI-D-16-0758.1

Ghannam, K., Nakai, T., Paschalis, A., Oishi, C.A., Kotani, A., Igarashi, Y., Kumagai, T., Katul, G.G., 2016. Persistence and memory timescales in root-zone soil moisture dynamics. Water Resour. Res. 52, 1427–1445. https://doi.org/10.1002/2015WR017983

Guo, Z., Dirmeyer, P.A., Koster, R.D., Sud, Y.C., Bonan, G., Oleson, K.W., Chan, E., Verseghy, D., Cox, P., Gordon, C.T., McGregor, J.L., Kanae, S., Kowalczyk, E., Lawrence, D., Liu, P., Mocko, D., Lu, C.-H., Mitchell, K., Malyshev, S., McAvaney, B., Oki, T., Yamada, T., Pitman, A., Taylor, C.M., Vasic, R., Xue, Y., 2006. GLACE: The Global Land–Atmosphere Coupling Experiment. Part II: Analysis. J. Hydrometeor 7, 611–625. https://doi.org/10.1175/JHM511.1

Hersbach, H., Bell, B., Berrisford, P., Hirahara, S., Horányi, A., Muñoz-Sabater, J., Nicolas, J., Peubey, C., Radu, R., Schepers, D., Simmons, A., Soci, C., Abdalla, S., Abellan, X., Balsamo, G., Bechtold, P., Biavati, G., Bidlot, J., Bonavita, M., Chiara, G., Dahlgren, P., Dee, D., Diamantakis, M., Dragani, R., Flemming, J., Forbes, R., Fuentes, M., Geer, A., Haimberger, L., Healy, S., Hogan, R.J., Hólm, E., Janisková, M., Keeley, S., Laloyaux, P., Lopez, P., Lupu, C., Radnoti, G., Rosnay, P., Rozum, I., Vamborg, F., Villaume, S., Thépaut, J., 2020. The ERA5 global reanalysis. Q.J.R. Meteorol. Soc. 146, 1999–2049. https://doi.org/10.1002/qj.3803

Hu, G., Jia, L., 2015. Monitoring of Evapotranspiration in a Semi-Arid Inland River Basin by Combining Microwave and Optical Remote Sensing Observations. Remote Sensing 7, 3056–3087. https://doi.org/10.3390/rs70303056

Huffman, G.J., Stocker, E.F., Bolvin, D.T., Nelkin, E.J., Tan, J., Savtchenko, A., 2019. GPM IMERG Final Precipitation L3 1 day 0.1 degree x 0.1 degree V06.

Katul, G.G., Porporato, A., Daly, E., Oishi, A.C., Kim, H.-S., Stoy, P.C., Juang, J.-Y., Siqueira, M.B., 2007. On the spectrum of soil moisture from hourly to interannual scales: SPECTRUM OF SOIL MOISTURE CONTENT. Water Resour. Res. 43. https://doi.org/10.1029/2006WR005356

Kim, H., Lakshmi, V., 2019. Global Dynamics of Stored Precipitation Water in the Topsoil Layer From Satellite and Reanalysis Data. Water Resources Research 55, 3328–3346. https://doi.org/10.1029/2018WR023166

Kobayashi, S., Ota, Y., Harada, Y., Ebita, A., Moriya, M., Onoda, H., Onogi, K., Kamahori, H., Kobayashi, C., Endo, H., Miyaoka, K., Takahashi, K., 2015. The JRA-55 Reanalysis: General Specifications and Basic Characteristics. Journal of the Meteorological Society of Japan 93, 5–48. https://doi.org/10.2151/jmsj.2015-001

Konings, A.G., Piles, M., Rötzer, K., McColl, K.A., Chan, S.K., Entekhabi, D., 2016. Vegetation optical depth and scattering albedo retrieval using time series of dual-polarized L-band radiometer observations. Remote Sensing of Environment 172, 178–189. https://doi.org/10.1016/j.rse.2015.11.009

Koster, R.D., 2004. Regions of Strong Coupling Between Soil Moisture and Precipitation. Science 305, 1138–1140. https://doi.org/10.1126/science.1100217

Koster, R.D., Dirmeyer, P.A., Hahmann, A.N., Ijpelaar, R., Tyahla, L., Cox, P., Suarez, M.J., 2002. Comparing the Degree of Land–Atmosphere Interaction in Four Atmospheric General Circulation Models. J. Hydrometeor. 3, 363–375. https://doi.org/10.1175/1525-7541(2002)003<0363:CTDOLA>2.0.CO;2

Koster, R.D., Schubert, S.D., Suarez, M.J., 2009. Analyzing the Concurrence of Meteorological Droughts and Warm Periods, with Implications for the Determination of Evaporative Regime. Journal of Climate 22, 3331–3341. https://doi.org/10.1175/2008JCLI2718.1

Koster, R.D., Suarez, M.J., 2001. Soil moisture memory in climate models. J. Climate 2, 558–570. https://doi.org/10.1175/1525-7541(2001)002<0558:SMMICM>2.0.CO;2

Koster, R.D., Sud, Y.C., Guo, Z., Dirmeyer, P.A., Bonan, G., Oleson, K.W., Chan, E., Verseghy, D., Cox, P., Davies, H., Kowalczyk, E., Gordon, C.T., Kanae, S., Lawrence, D., Liu, P., Mocko, D., Lu, C.-H., Mitchell, K., Malyshev, S., McAvaney, B., Oki, T., Yamada, T., Pitman, A., Taylor, C.M., Vasic, R., Xue, Y., 2006. GLACE: The Global Land–Atmosphere Coupling Experiment. Part I: Overview. J. Hydrometeor 7, 590–610. https://doi.org/10.1175/JHM510.1

Li, Bailing, Beaudoing, H., Rodell, M., NASA/GSFC/HSL, 2020. GLDAS Catchment Land Surface Model L4 daily 0.25 x 0.25 degree GRACE-DA1 Early Product, Version 2.2. https://doi.org/10.5067/IIU5JWU2AGRP

Liu, X., Yuan, X., Zhu, E., 2021. Global warming induces significant changes in the fraction of stored precipitation in the surface soil. Global and Planetary Change 103616. https://doi.org/10.1016/j.gloplacha.2021.103616

Martínez-Fernández, J., González-Zamora, A., Almendra-Martín, L., 2020. Soil moisture memory and soil properties: An analysis with the stored precipitation fraction. Journal of Hydrology 125622. https://doi.org/10.1016/j.jhydrol.2020.125622

McColl, K.A., Alemohammad, S.H., Akbar, R., Konings, A.G., Yueh, S., Entekhabi, D., 2017a. The global distribution and dynamics of surface soil moisture. Nature Geosci 10, 100–104. https://doi.org/10.1038/ngeo2868

McColl, K.A., He, Q., Lu, H., Entekhabi, D., 2019a. Short-Term and Long-Term Surface Soil Moisture Memory Time Scales Are Spatially Anticorrelated at Global Scales. J. Hydrometeor. 20, 1165–1182. https://doi.org/10.1175/JHM-D-18-0141.1

McColl, K.A., He, Q., Lu, H., Entekhabi, D., 2019b. Short-Term and Long-Term Surface Soil Moisture Memory Time Scales Are Spatially Anticorrelated at Global Scales. J. Hydrometeor. 20, 1165–1182. https://doi.org/10.1175/JHM-D-18-0141.1

McColl, K.A., Wang, W., Peng, B., Akbar, R., Short Gianotti, D.J., Lu, H., Pan, M., Entekhabi, D., 2017b. Global characterization of surface soil moisture drydowns: SURFACE SOIL MOISTURE DRYDOWN ANALYSIS. Geophys. Res. Lett. 44, 3682–3690. https://doi.org/10.1002/2017GL072819

Miralles, D.G., Gentine, P., Seneviratne, S.I., Teuling, A.J., 2019. Land-atmospheric feedbacks during droughts and heatwaves: state of the science and current challenges: Land feedbacks during droughts and heatwaves. Ann. N.Y. Acad. Sci. 1436, 19–35. https://doi.org/10.1111/nyas.13912

Miralles, D.G., Teuling, A.J., van Heerwaarden, C.C., Vilà-Guerau de Arellano, J., 2014. Mega-heatwave temperatures due to combined soil desiccation and atmospheric heat accumulation. Nature Geosci 7, 345–349. https://doi.org/10.1038/ngeo2141
Mu, Q., Heinsch, F.A., Zhao, M., Running, S.W., 2007. Development of a global evapotranspiration algorithm based on MODIS and global meteorology data. Remote Sensing of Environment 111, 519–536. https://doi.org/10.1016/j.rse.2007.04.015
Mu, Q., Zhao, M., Steven, W., 2014. Running and Numerical Terradynamic Simulation Group: MODIS Global Terrestrial Evapotranspiration (ET) Product MOD16A2 Collection 5.
Niu, G.-Y., Yang, Z.-L., Mitchell, K.E., Chen, F., Ek, M.B., Barlage, M., Kumar, A., Manning, K., Niyogi, D., Rosero, E., Tewari, M., Xia, Y., 2011. The community Noah land surface model with multiparameterization options (Noah-MP): 1. Model description and evaluation with local-scale measurements. J. Geophys. Res. 116, D12109. https://doi.org/10.1029/2010JD015139
Pastorello, G., Trotta, C., Canfora, E., Chu, H., Papale, D., 2020. The FLUXNET2015 dataset and the ONEFlux processing pipeline for eddy covariance data. Scientific Data 7. https://doi.org/10.1038/s41597-020-0534-3
Saxton, K.E., Rawls, W.J., 2006. Soil Water Characteristic Estimates by Texture and Organic Matter for Hydrologic Solutions. Soil Sci. Soc. Am. J. 70, 1569–1578. https://doi.org/10.2136/sssaj2005.0117
Schwingshackl, C., Hirschi, M., Seneviratne, S.I., 2017. Quantifying Spatiotemporal Variations of Soil Moisture Control on Surface Energy Balance and Near-Surface Air Temperature. Journal of Climate 30, 7105–7124. https://doi.org/10.1175/JCLI-D-16-0727.1
Seneviratne, S.I., Corti, T., Davin, E.L., Hirschi, M., Jaeger, E.B., Lehner, I., Orlowsky, B., Teuling, A.J., 2010. Investigating soil moisture–climate interactions in a changing climate: A review. Earth-Science Reviews 99, 125–161. https://doi.org/10.1016/j.earscirev.2010.02.004
Seneviratne, S.I., Lüthi, D., Litschi, M., Schär, C., 2006. Land–atmosphere coupling and climate change in Europe. Nature 443, 205–209. https://doi.org/10.1038/nature05095
Shangguan, W., Dai, Y., Duan, Q., Liu, B., Yuan, H., 2014. A global soil data set for earth system modeling. J. Adv. Model. Earth Syst. 6, 249–263. https://doi.org/10.1002/2013MS000293
Williams, I.N., Torn, M.S., 2015. Vegetation controls on surface heat flux partitioning, and land-atmosphere coupling: VEGETATION AND LAND-ATMOSPHERE COUPLING. Geophys. Res. Lett. 42, 9416–9424. https://doi.org/10.1002/2015GL066305
Yang, Z.-L., Niu, G.-Y., Mitchell, K.E., Chen, F., Ek, M.B., Barlage, M., Longuevergne, L., Manning, K., Niyogi, D., Tewari, M., Xia, Y., 2011. The community Noah land surface model with multiparameterization options (Noah-MP): 2. Evaluation over global river basins. J. Geophys. Res. 116, D12109. https://doi.org/10.1029/2010JD015139
Yao, P., Lu, H., Shi, J., Zhao, T., Yang, K., Cosh, M.H., Gianotti, D.J.S., Entekhabi, D., 2021. A long term global daily soil moisture dataset derived from AMSR-E and AMSR2 (2002–2019). Sci Data 8, 143. https://doi.org/10.1038/s41597-021-00925-8
Zhang, Y., Kong, D., Gan, R., Chiew, F.H.S., McVicar, T.R., Zhang, Q., Yang, Y., 2019. Coupled estimation of 500 m and 8-day resolution global evapotranspiration and gross primary

production in 2002–2017. Remote Sensing of Environment 222, 165–182. https://doi.org/10.1016/j.rse.2018.12.031

Zhao, W.L., Gentine, P., Reichstein, M., Zhang, Y., Zhou, S., Wen, Y., Lin, C., Li, X., Qiu, G.Y., 2019. Physics-Constrained Machine Learning of Evapotranspiration. Geophysical Research Letters 46, 14496–14507. https://doi.org/10.1029/2019GL085291

Zhou, S., Yu, B., Zhang, L., Huang, Y., Pan, M., Wang, G., 2016. A new method to partition climate and catchment effect on the mean annual runoff based on the Budyko complementary relationship: PARTITIONING THE CLIMATE AND CATCHMENT EFFECT ON RUNOFF. Water Resour. Res. 52, 7163–7177. https://doi.org/10.1002/2016WR019046

Earth's Future

Supporting Information for

Soil Moisture Memory in Commonly-used Land Surface Models Differ Significantly from SMAP Observation

Qing He[1], Hui Lu[1,2] and Kun Yang[1]

[1]Ministry of Education Key Laboratory for Earth System Modeling and the Department of Earth System Science, Tsinghua University, Beijing, 100084, China

[2]Ministry of Education Ecological Field Station for East Asian Migratory Birds, Beijing, 100084, China

Contents of this file

Introduction

This document contains supplementary figures and tables supporting the main context.

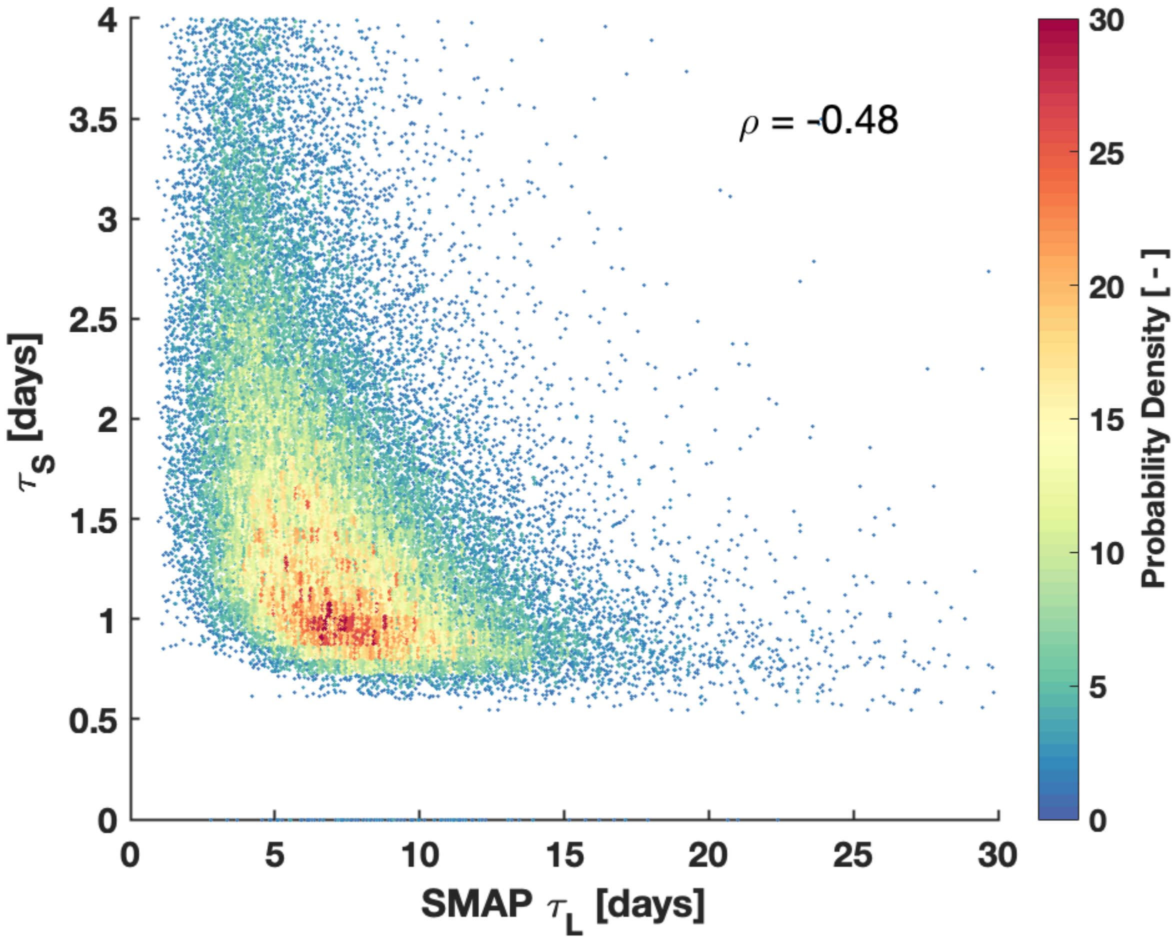

Figure S1. Scatter plot of energy-limited (τ_S) and water-limited soil memory (τ_L)

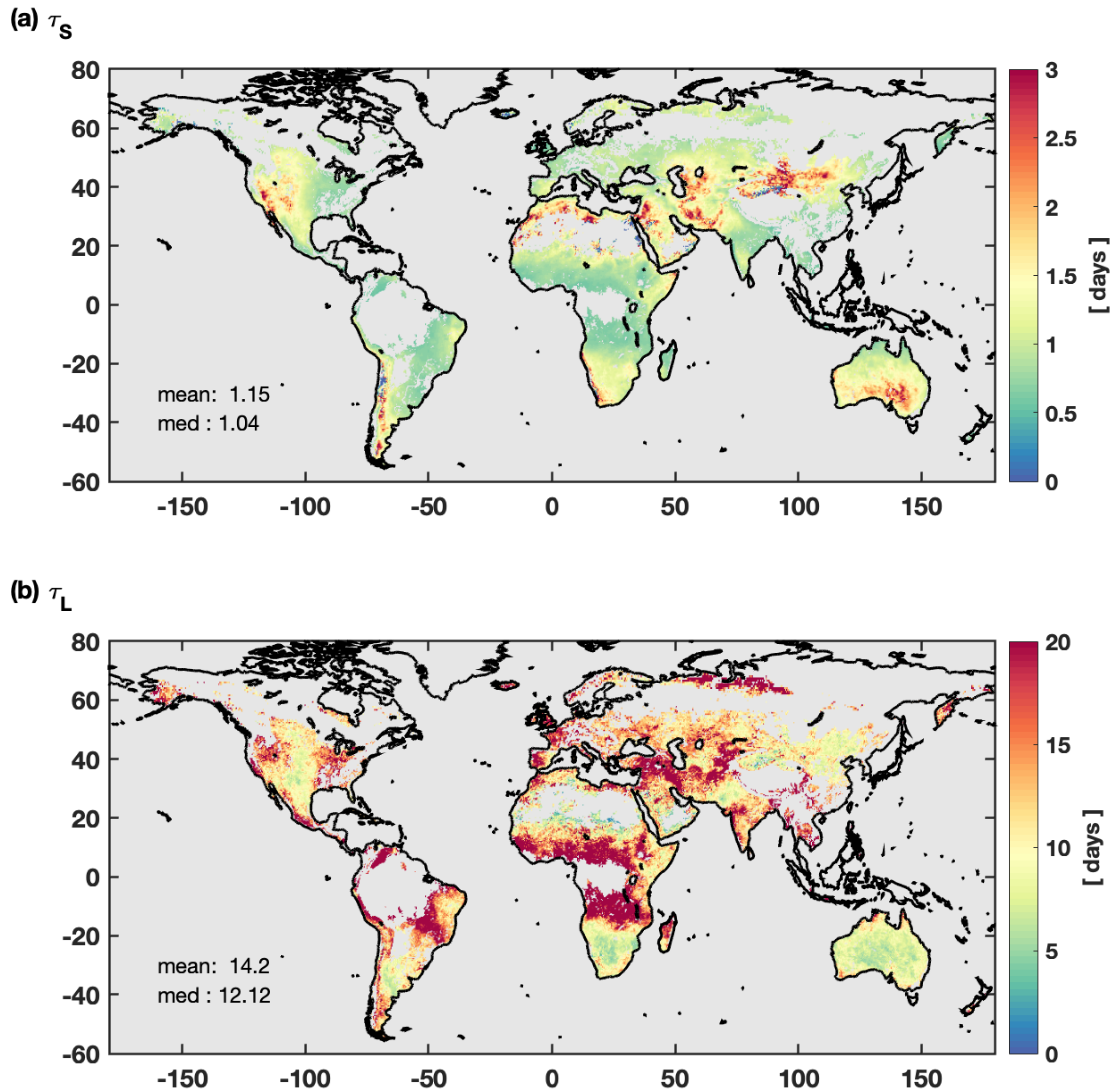

Figure S2. Global distribution of multi-model-mean τ_S (a) and τ_L (b) from six reanalysis datasets

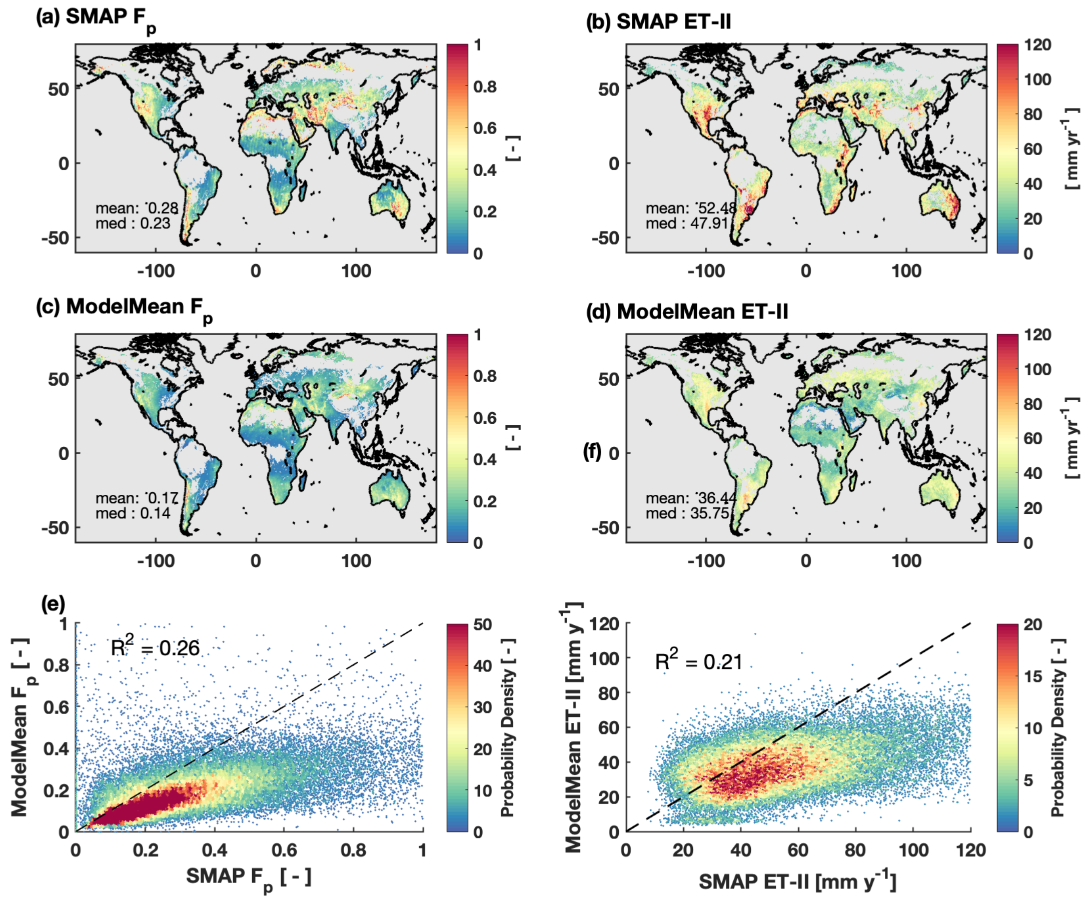

Figure S3. Same as Figure 7 but for all datasets.

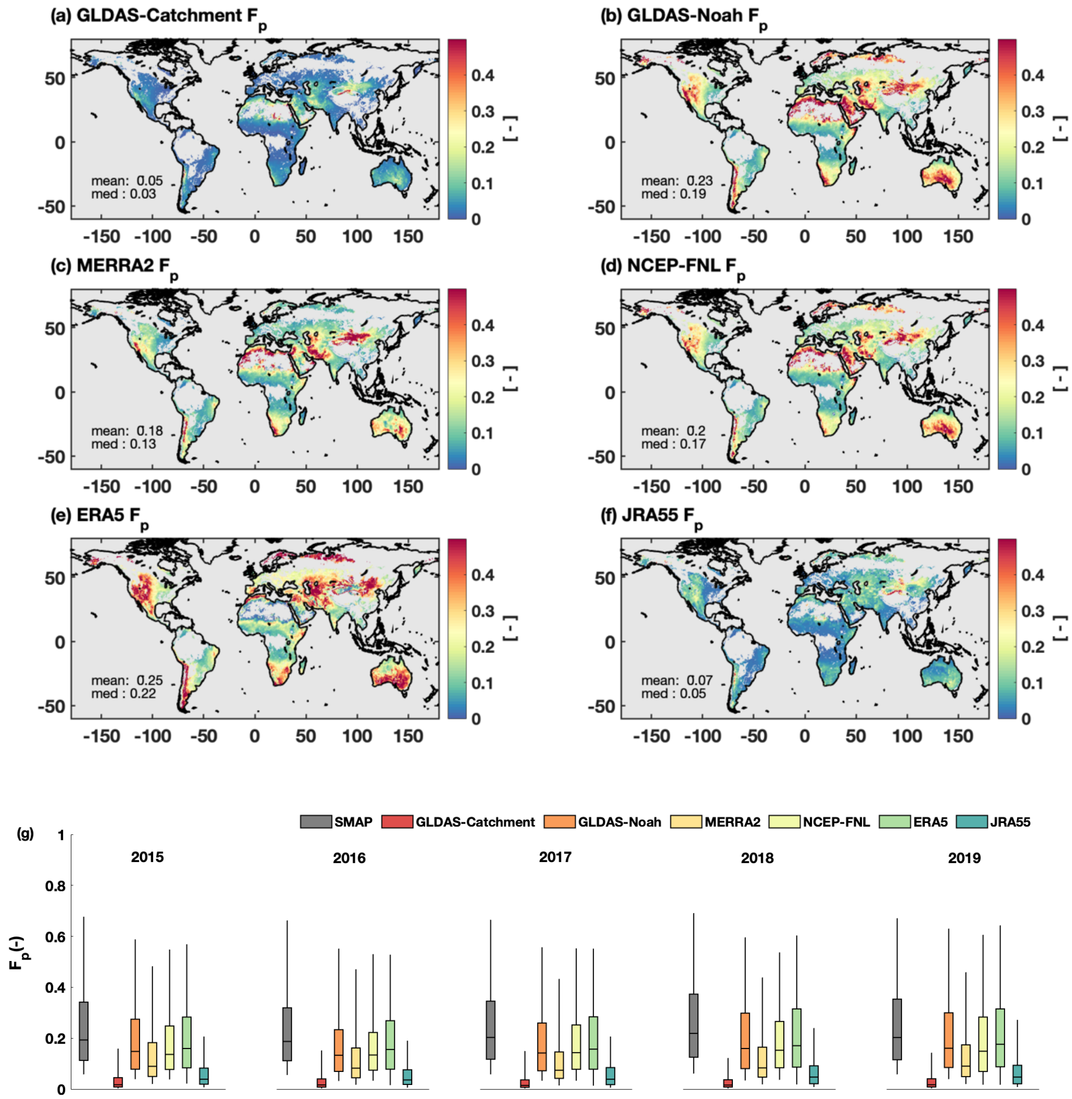

Figure S4 Global distribution of precipitation fraction F_p from individual dataset (a – f) and comparison of their annual variability (g)

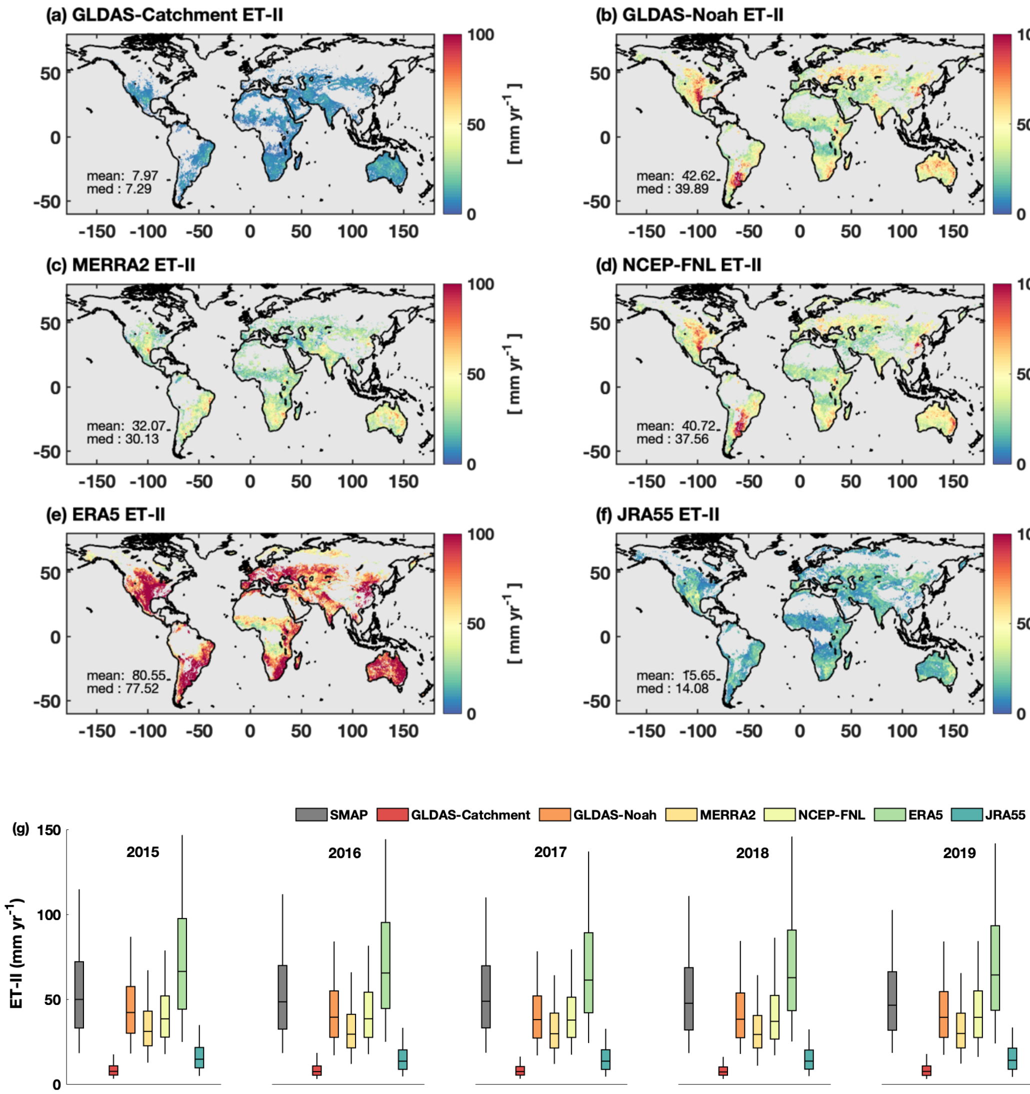

Figure S5 Same as Figure S4 but for Stage-II ET

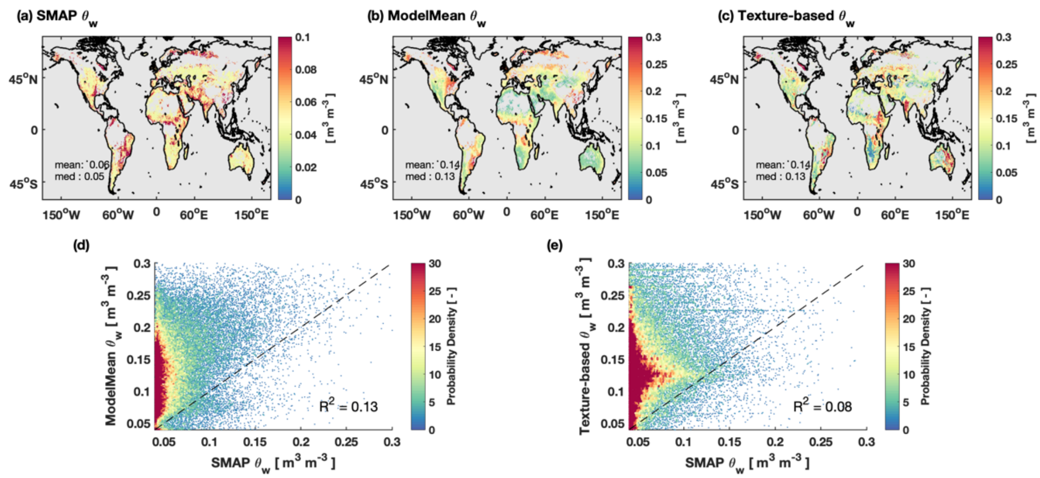

Figure S6 Global distribution of soil wilting point θ_w from satellite estimation (a), multi-model means(b), and from texture-based result (c); (d) and (e) indicates scatter plot of multi-model mean against satellite estimation and texture-based (SR06 scheme) result, respectively.

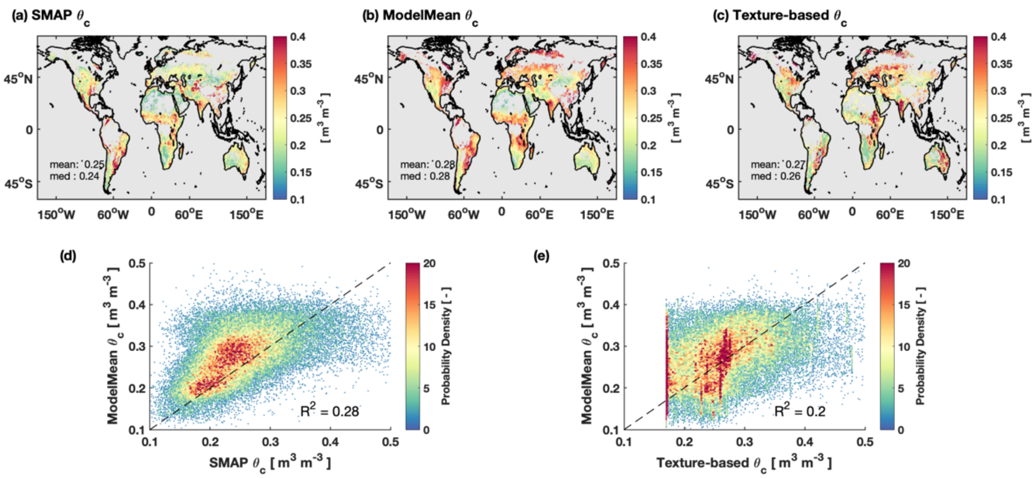

Figure S7 Same as Figure S6 but for soil critical point θ_c

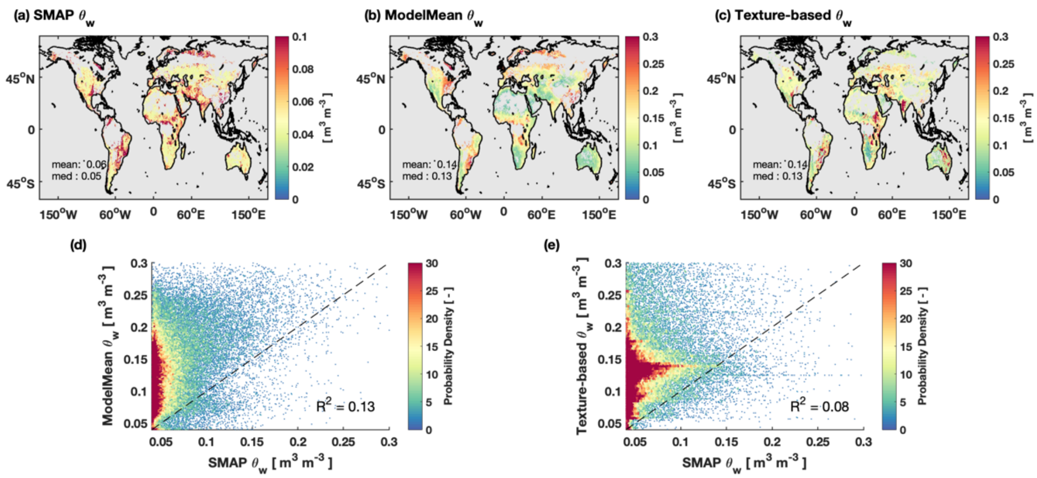

Figure S8 Global distribution of soil wilting point θ_w from satellite estimation (a), multi-model means(b), and from texture-based result (c); (d) and (e) indicates scatter plot of multi-model mean against satellite estimation and texture-based (Clapp and Hornberger (1978) scheme) result, respectively.

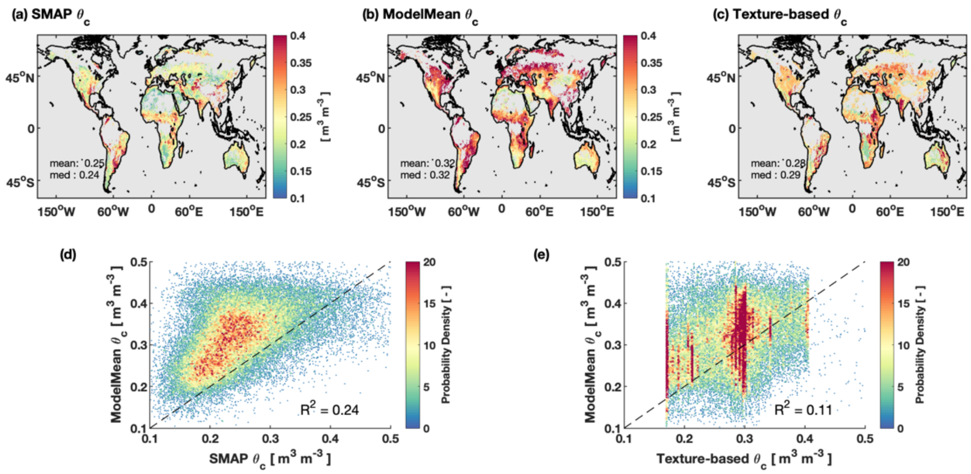

Figure S9 Same as Figure S8 but the texture-based θ_c is calculated from Clapp and Hornberger (1978) scheme.

Table S1 Pedotransfer Function from Saxton and Rawls (2006) (left column) and Clapp and Hornberger (1978) (right column). C, S, OC refers to soil clay content (%), sand content (%), and organic carbon (%) respectively.

	PTF-SR06	PTF-CH
Soil Wilting Pointθ_w	$\theta_w = \theta_{1500t} + (0.14\theta_{1500t} - 0.02)$ $\theta_{1500t} = -0.024S + 0.487C + 0.006OC + 0.005(S*OC) - 0.013(C*OC) + 0.068(S*OC) + 0.031$	$\theta_w = (\frac{15.0}{\alpha})^{(\frac{1}{\beta})}$ $\alpha = \exp(-4.36 - 0.0715C - 4.88e - 4S^2 - 4.285e - 5S^2C)$ $\beta = -3.140 - 0.0022C^2 - 3.484e - 5S^2C$
Critical Point θ_{ref}	$\theta_{ref} = \theta_{33t} + 1.283\theta_{33t}^2 - 0.374\theta_{33t} - 0.015$ $\theta_{33t} = -0.251S + 0.195C + 0.011OC + 0.006(S*OC) - 0.027(C*OC) + 0.452(S*OC) + 0.299$	$\theta_{ref} = 0.01(11.83 + 0.96C - 0.008C^2)$
Saturated Point θ_{sat}	$\theta_{sat} = \theta_{33} + \theta_{s-33} - 0.097S + 0.043$ $\theta_{s-33} = \theta_{(s-33)t} + 0.636\theta_{(s-33)t} - 0.107$ $\theta_{(s-33)t} = 0.278S + 0.034C + 0.022OC + 0.018(S*OC) - 0.027(C*OC) - 0.584(S*OC) + 0.078$	$\theta_{sat} = 0.489 - 0.00126S$
$bexp(-)$	$bexp = \frac{3.8167}{\log(\theta_{ref}) - \log(\theta_w)}$	$bexp = 2.91 + 0.159C$
Saturated Soil Matric Potential ψ_{sat} (m)	$\psi_{sat} = \psi_{et} + 0.02\psi_{et}^2 - 0.113\psi_{et} - 0.70$ $\psi_{sat} = \psi_{sat} * 0.101997$ $\psi_{et} = -21.67S - 27.93C - 81.97\theta_{s-33} + 71.12(S*\theta_{s-33}) + 8.29(C*\theta_{s-33}) + 14.05(S*C) + 27.16$	$\psi_{sat} = 10(10^{(1.88-0.131S)})/1000$
Saturated soil conductivity κ_{sat} (m/s)	$\kappa_{sat} = 1930(\theta_{sat} - \theta_{33})^{1-bexp}$ $\kappa_{sat} = \kappa_{sat}/3600000$	$\kappa_{sat} = 0.0070556(10^{(-0.884-0.0153S)})$ $\kappa_{sat} = \kappa_{sat}/1000$

Saturated soil diffusivity $\lambda_{sat}(m2/s)$	$\lambda_{sat} = \frac{\kappa_{sat} \cdot \psi_{sat} \cdot bexp}{\theta_{sat}}$	$\lambda_{sat} = \frac{\kappa_{sat} \cdot \psi_{sat} \cdot bexp}{\theta_{sat}}$
Quartz	*Quartz = sand/2*	*Quartz = sand/2*